Paleomagnetism of the Tsumis Group in the Kalahari foreland of the Damara orogen, Namibia

Dana Polomski
Advisor: David A.D. Evans, Yale University
Second Reader: Lyle L. Nelson, Carleton University

A Senior Thesis presented to the faculty of the Department of Earth and Planetary Sciences, Yale University, in partial fulfillment of the Bachelor's Degree.

Department of Earth & Planetary Sciences
Yale University

1 MAY 2024
[Revised May 5, 2024]

Contents

Acknowledgements

My deepest gratitude goes to Dave Evans, my advisor, for allowing me the freedom to take complete ownership of this project while making himself available to me when I am doing my best to turn it into a dumpster fire. His knowledge of not just paleomagnetism, but geology broadly, is incredibly vast and has prevented me from making many wrong turns. I thank my second reader, Lyle Nelson, for his invaluable support in the field, limitless knowledge of geology and stick bugs, and for being willing to read the witchcraft that is a paleomagician's thesis.

Terrence, who graciously allowed us to sample on his beautiful farm, and his farm manager Frankie, were a wonderful and too brief addition to all of the field team's lives.

This study would not have been possible without the support of colleagues from Namibia, particularly Ben Mapani and Ambitious Lifasi, who were unwaveringly positive even as the entire field team worked through a two-week-long bout of definitely-not-COVID, and Charlie Hoffman, who is thanked for enlightening fireside conversations about geology. I am so lucky to have had the pleasure of working with Johanna Salminen - indisputably the hardest working and most patient woman in paleomagnetism. Jikai Ding's dark humor lightened my mood at many times in the field and lab. My lab mates who did not join us in the field (Phil, Thales, Yanan, Lexie, and Eliza) have provided endless support in many forms. Without the free dog care provided by my parents, Susan Fenn and Mark Polomski, I would never have been able to have the lifestyle of a field geologist. Last and certainly not least, I thank my partner in paleomag, James Pierce, who has given me unwavering support through the sweat, tears, and occasional blood involved in field work - there is no one else I would rather carry water up a mountain with.

Financial support is acknowledged from Yale University in the form of the Karen L. Von Damm '77 Undergraduate Research Fellowship, the Summer Experience Award, and David Evans' discretionary research fund. Additional financial support was supplied by the Northeastern section of the Geological Society of America in the form of the Stephen G. Pollock Undergraduate Research Grant.

Figures

1 Introduction

Paleogeography at any given time has vast implications on a variety of interlinked Earth systems, such as mantle dynamics, climate impacts, and the evolution of life itself (Jagoutz et al., 2016; Lee et al., 2015; Macdonald et al., 2019; Meert, 2012; Mitchell et al., 2021). Supercontinents, which have existed at least three times throughout Earth's history, are one of the most well-known and best studied aspects of paleogeography (Fig. 1). The middle of the three supercontinent siblings, Rodinia, is well established to have begun assembling during the late Mesoproterozoic, with onset of the rifting and breakup phase of its cycle by the latest Tonian (Cawood and Pisarevsky, 2017; Cawood et al., 2016; Ding et al., 2021; Evans, 2021; Evans et al., 2016; Eyster et al., 2017, 2020; Hanson et al., 2004; Hoffman, 1999, 2021; Jing et al., 2020; Kasbohm et al., 2016; Li et al., 2019; Li et al., 2008; Li et al., 2023; Mitchell et al., 2021; Pisarevsky et al., 2003; Pu et al., 2022, 2023, and many others). However, the position of some cratons within Rodinia are not resolvable with the currently available paleomagnetic and geologic datasets. In particular, the placement of the Kalahari craton has remained enigmatic due to a paucity of high-quality published paleomagnetic poles from the earliest Tonian to the beginning of the Phanerozoic, a fact exasperated by the lack of definitively correlatable geologic evidence (e.g., temporally and metamorphically linked orogenies or temporally, geometrically, and geochemically linked radiating dyke swarms) to connect Kalahari to any particular craton during the same time period (Gumsley et al., 2023; Li et al., 2023; Merdith, Collins, et al., 2017; Torsvik et al., 2012).

The earliest Rodinia model placed Kalahari to the south of Laurentia - a position which is still a viable and parsimonious solution to the Rodinia puzzle today that is supported by paleomagnetic and geologic evidence (Ding et al., 2021; Eyster et al., 2020; Hoffman, 1991; Jing et al., 2020, 2021; Li et al., 2013; Merdith, Williams, et al., 2017; Pu et al., 2023; Zhao et al., 2018). A variety of other positions for Kalahari in Rodinia have been put forth over the thirty-three years since the model of Hoffman, 1991 was proposed, including Kalahari to the east of Laurentia and Kalahari directly south of Australia with Australia directly south of Laurentia (Dalziel, 1997; Meert and Torsvik, 2003; Pisarevsky et al., 2003). These alternative models have largely been discarded as inconsistent with more recent paleomagnetic, geologic, and plate kinematic evidence (Li et al., 2008). Recently, a paleomagnetically and geologically viable "Kalahari-in-the-north" model has been proposed that places Kalahari on Laurentia's northern margin instead of its southern (Gumsley et al., 2023; Fig. 2). While this model would require a series of complicated place motions, it is nonetheless possible with the plate movement speeds allowed by proposed Precambrian kinematic controls and true polar wander rates allowed by theoretical Precambrian mantle viscosity (Gerya, 2014; Gumsley et al., 2023; Rose and Buffett, 2017; Zahirovic et al., 2015).

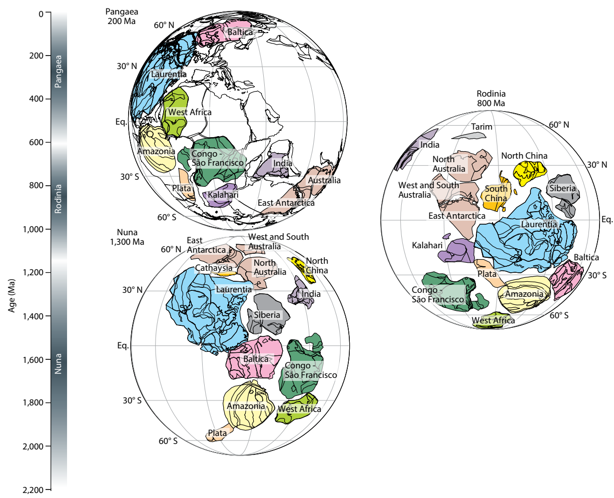

Figure 1: The supercontinent cycle. Modified from Mitchell et al., 2021.

Kalahari's paleolatitude and placement during Rodinia and its subsequent dispersal could have significant climatic and geodynamic consequences. Rodinia is an oddity among supercontinents. It is the only of the three established supercontinents to have experienced low-latitude glaciations (Hoffman et al., 1998, 2017; Kirschvink, 1992). The Snowball Earth glaciations themselves may have been substantially driven by the unique paleogeography of Rodinia. Rodinia-era cratons were situated dominantly at low latitudes (Evans, 2000). As weathering rates are significantly higher in these low tropical and subtropical latitudes than in the drier high latitudes, the emplacement at the equator of what may have been the largest large igneous province (LIP) in Earth history - northern Laurentia's Franklin LIP - has been invoked as drawing down enough CO_2 through weathering processes to have been a consequential driver for initiation of the ca. 717 Ma Sturtian Snowball Earth (Cox et al., 2016; Donnadieu et al., 2004; Dufour et al., 2023; Goddéris et al., 2003; Macdonald and Swanson-Hysell, 2023; Macdonald et al., 2010; Pu et al., 2022). Spatially and temporally correlating LIPs that are broadly contemporaneous with the ca. 719 Franklin LIP (Fig. 4), as has been proposed with the ca. 720 Ma Irkutsk LIP in Siberia and ca. 724-712 Mutare-Fingeren LIP in Kalahari and East Antarctica, would further support this "fire and ice" glaciation trigger by increasing both the potential subaerial area and total volume of a directly pre-Sturtian low-latitude LIP. However, the paleomagnetic and high-precision geochronological data to confirm these correlations are lacking (Ernst et al., 2023; Gumsley et al., 2023). As the warmest and wettest parts of modern Earth are within 10° of the equator, in order to test the paleoclimatic significance of Mutare-Fingeren LIP weathering, precise placement of Kalahari with respect to Laurentia is imperative given Laurentia's comparatively well constrained movement through the Neoproterozoic (Swanson-Hysell, 2021). Linking the Franklin LIP and Mutare-Fingeren LIP would require Kalahari to have been positioned on Laurentia's northern margin and have traveled quickly through space

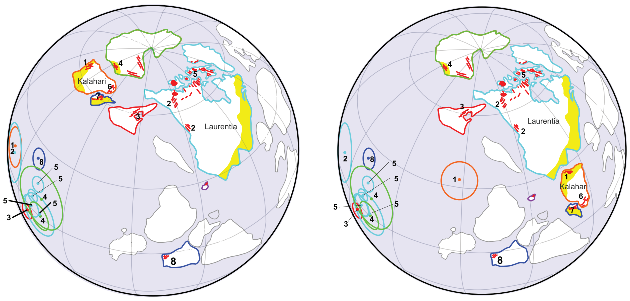

Kalahari-in-the-north Rodinia model. Kalahari-in-the-south Rodinia model.

Figure 2: Placements for the Kalahari craton in Rodinia at 800 Ma. Modified from Gumsley et al., 2023. Kalahari pole "1" from ca. 795 Gannakouriep dyke swarm (Bartholomew, 2008, unpublished master's thesis; Evans and Hanson, in prep).

towards its eventual collision with the Congo and Plata cratons during the later continental assembly of Gondwana (Fig. 4).

Alternatively, the traditional model of "Kalahari-in-the-south" links Kalahari to southern Laurentia via the coeval ca. 1090-1060 Ma Namaqua-Natal belt in Kalahari and the Grenville belt in Laurentia, as well as a link between Laurentia's Mount Rogers and Kalahari's Rosh Pinah rift-related successions, which leaves Kalahari with similar neighbors in both Rodinia and the later Gondwana assembly - consistent with classical Wilson Cycle dynamics (Jacobs et al., 2008; Li et al., 2023; Pu et al., 2023; Swanson-Hysell et al., 2015). This traditional model does not preclude Kalahari from being at low latitudes in Rodinia, but differing placement of cratons within supercontinents do require significantly different plate motions and mantle dynamics (e.g., introversion being consistent with the closure of interior oceans, extroversion being consistent with the closure of exterior oceans, and orthoversion's "subduction girdle" and mantle down welling).

Given that paleomagnetism is the only currently available quantitative tool for determining paleolatitude in the Precambrian, and the paucity of "high-quality" (as determined by the Nordic Paleomagnetic workshop grading system) published paleomagnetic data from ca. 1000 Ma to ca. 500 Ma for Kalahari (Fig. 3), it is clear that new data is required to answer these unresolved questions. A data set that fills the Kalahari craton's 500 million year gap in "high-quality", published, and temporally well-constrained paleomagnetic poles is needed to resolve whether the Kalahari craton is spatially linked to northern Laurentia in Rodinia by LIPs derived from the same mantle plume or if Kalahari was connected to southern Laurentia in Rodinia by a Namaqua-Natal-Grenville orogeny and geologic associations between Mount Rogers and Rosh Pinah rift-related volcanic complexes (Gumsley et al., 2023; Pu et al., 2023; Swanson-Hysell et al., 2015). However, acquiring primary paleomagnetic data for this time period has proved to be difficult. Many Mesoproterozoic and Neoproterozoic mafic rocks in Kalahari are pervasively paleomagnetically overprinted by the effects of

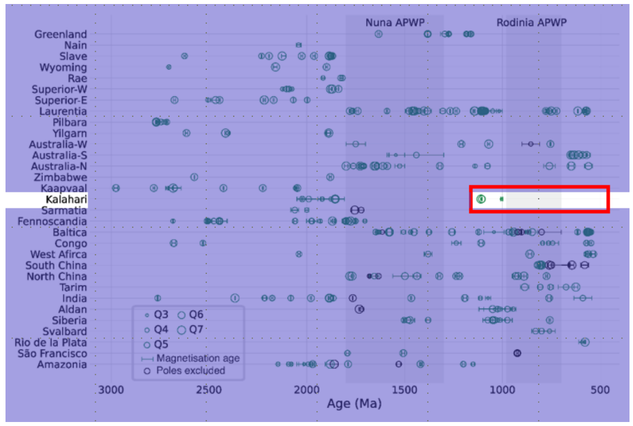

Figure 3: Large green circles show highest-quality paleomagnetic poles (as determined by Nordic Paleomagnetic Workshop grade), smaller green circles show "lower quality" published poles. Poles shown are used in the global reconstruction model of Li et al., 2023, which uses the "Kalahari-in-the-south" traditional model. Note complete lack of data from ca. 1000 Ma to 500 Ma. This model is only one option, and is shown here to highlight the general lack of paleomagnetic data (note that more exists that is not used in this model, e.g., ca. 795 Ma Gannakouriep dyke swarm of Bartholomew, 2008 and Evans and Hanson, in prep; ca. 1100 Ma Aubures Formation of Kasbohm et al., 2016; ca. 795 Pre-Nama dykes of Piper, 1975). Modified from Li et al., 2023. See de Kock et al., 2021 for a thorough discussion of Precambrian Kalahari paleomagnetic poles; Torsvik et al., 2012 for Phanerozoic Kalahari paleomagnetic poles.

the Ediacaran and Cambrian collision between the Kalahari and Congo cratons that resulted in the Damara orogeny.

While most prospective sedimentary sequences in Kalahari lack chronostratigraphic age constraints, have mineralogical compositions unlikely to be suitable for paleomagnetism, or both, preliminary data from the Doornpoort and Opdam Formations within the Rehoboth Basement Inlier could imply ca. 1100 Ma syn-folding magnetization, contemporaneous with ca. 1100 Ma syn-folding magnetization implied by paleomagnetic data from the potentially correlative Aubures Formation of the Mesoproterozoic Sinclair Supergroup to the south (Chung-Halpern, 2021; Kasbohm et al., 2016; Mai, 2021). Additionally, a previously published Doornpoort paleomagnetic pole from potentially post-folding magnetization (Fig. 46, PIP pole) does not fall on the established apparent polar wander path for Kalahari - bearing the question when and where Kalahari was when the magnetization occurred (given that this data fails the paleomagnetic fold test, but does not fall anywhere on Kalahari's known post-1100 Ma apparent polar wander path), or if it instead resulted from vector component mixing (Piper, 1975). Answering either question could yield meaningful information regarding Kalahari's placement within the broader configuration of Rodinia.

1.1 Geologic Context

On the northwestern corner of the modern-day Kalahari craton, the Tsumis Group overlies the Nauzerus Group (Becker and Schalk, 2008). Zircons from rhyolites within the Nauzerus Group's Nückopf Formation

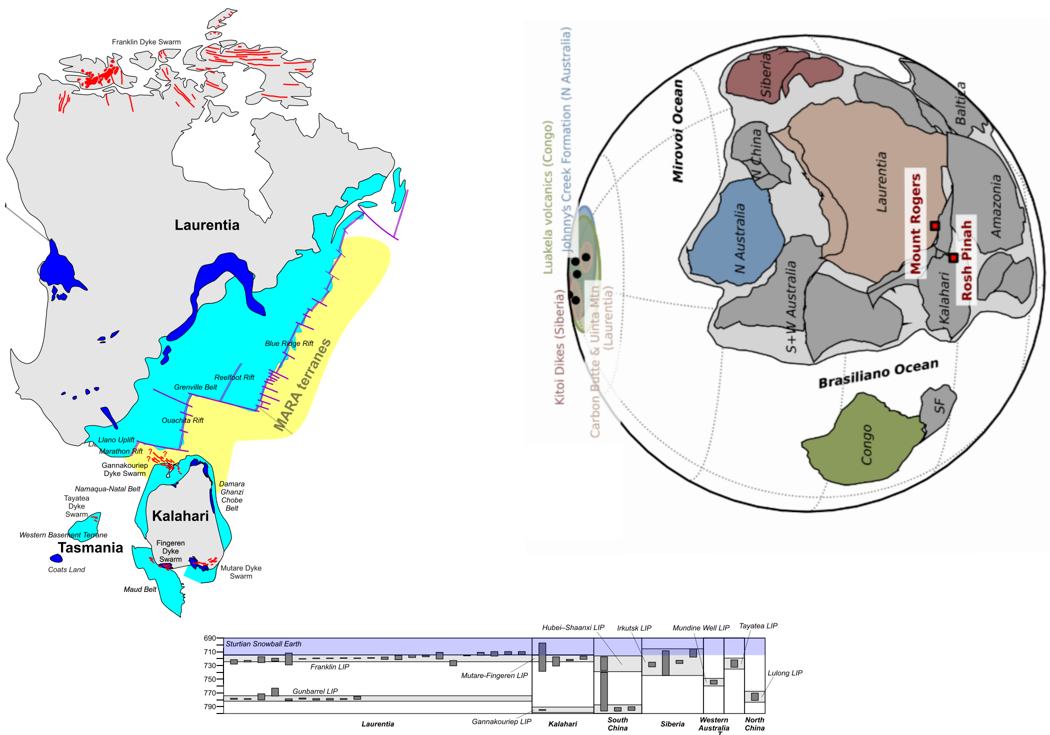

Figure 4: Two slightly different "Kalahari-in-the-south" models for placement of Kalahari with respect to Laurentia. Timing of global LIPs broadly contemporaneous with onset of Sturtian Snowball Earth in bottom of figure. Placement of Mutare-Fingeren dyke swarm and Gannakouriep dyke swarm in Kalahari in left figure. Modified from Gumsley et al., 2023; Pu et al., 2023.

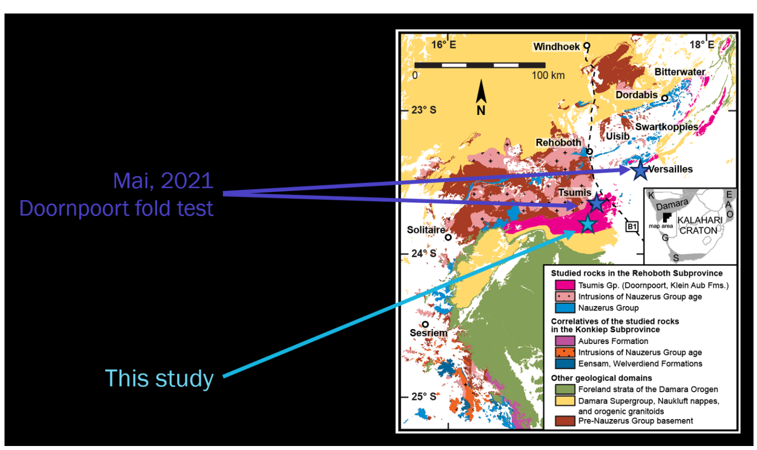

Figure 5: Regional geologic map showing the locations of this study and Mai, 2021. Modified from Lehmann et al., 2015.

have been dated at 1222 ± 46 Ma and 1210 ± 7 Ma (Schneider et al., 2004; Stoessel and Ziegler, 1989). The Nückopf Formation and the sedimentary rocks of the Grauwater Formation that overly and interfinger with it are intruded by plutons of the Gamsberg Granitic Suite, which has been variably described as representing either a volcanic arc or more broadly, an active margin setting but not specifically a volcanic arc (Becker and Schalk, 2008; Miller, 2012). The Gamsberg Granitic Suite has been dated by U-Pb zircon ages at 1210 ± 8 Ma, 1207 ± 15 Ma, 1194 ± 15 Ma and Rb/Sr whole rock ages at 1222 ± 45 Ma and 1190 ± 23 Ma (Pfurr et al., 1991; Reid et al., 1988; Seifert, 1986; Ziegler and Stoessel, 1993). The Langberg Formation, which overlies the Grauwater Formation and consists of conglomerate, quartzite, dacite to rhyolite ignimbrite and quartz-feldspar porphyry lava, is not intruded by the Gamsberg suite and has been dated by single zircon grains at 1100 ± 5 Ma and 1090 ± 15 Ma (Becker et al., 2005). While tectonic discrimination diagrams show the Langberg's volcanic rocks scattered between volcanic, arc, within-plate, and post-collision zones, they have generally been included in the ca. 1100 Ma Umkondo LIP that includes most late-Mesoproterozoic broad-scale magmatic activity in Kalahari (Becker et al., 2005; Hanson et al., 2006; Hanson et al., 2004). The Capricorn Granitic Suite is potentially comagmatic with the Langberg and has been dated at 1104 ± 20 Ma and 932 ± 50 Ma (Becker et al., 2005; Burger and Coertze, 1975). Stratigraphically overlying the Langberg Foirmation within the Nauzerus Group, the Opdam Formation has no radiometric age constraints but preliminary paleomagnetic data could suggest ca. 1100 Ma folding (Chung-Halpern, 2021). The youngest of the Nauzerus, the Skumok Formation, consists of sandstones interbedded with felsic volcanics (Lehmann et al., 2015).

The Tsumis Group has been variably suggested to occur within the Mesoproterozoic Sinclair Supergroup and be correlative to the ca. 1100 Ma Aubures Formation (e.g., Miller, 2012; Miller and Becker, 2008) to the south (notably giving syn-folding paleomagnetic results in the work of Kasbohm et al., 2016) or to represent the lowermost part of the Neoproterozoic Damara sequence (e.g, Becker et al., 2005; Corner and Durrheim, 2018; Hoffmann, 1989). Paleomagnetic data from the work of Mai, 2021 could imply that the Doornpoort was effected by the same purported non-Namaqua-Natal-Grenville ca. 1100 Ma folding event as the Opdam that is suggested in Chung-Halpern, 2021. However, syn-folding magnetization interpretations must be taken with some skepticism given that syn-folding paleomagnetic directions are not always representative of true paleomagnetic directions at the time of folding or indicative of syn-folding magnetization at all (Tauxe and Watson, 1994). Instead, they can be indicative of a rotation about a vertical axis (i.e., undetected structural complications; Fig. 7). There are currently no radiometric age constraints on the Tsumis Group. The Doornpoort Formation, which is the lowermost member of the Tsumis Group, has been suggested to lie unconformably over the Nauzerus Group.

The Tsumis Group consists of the red-bed successions of the Eskadron, Doornpoort, and Klein Aub

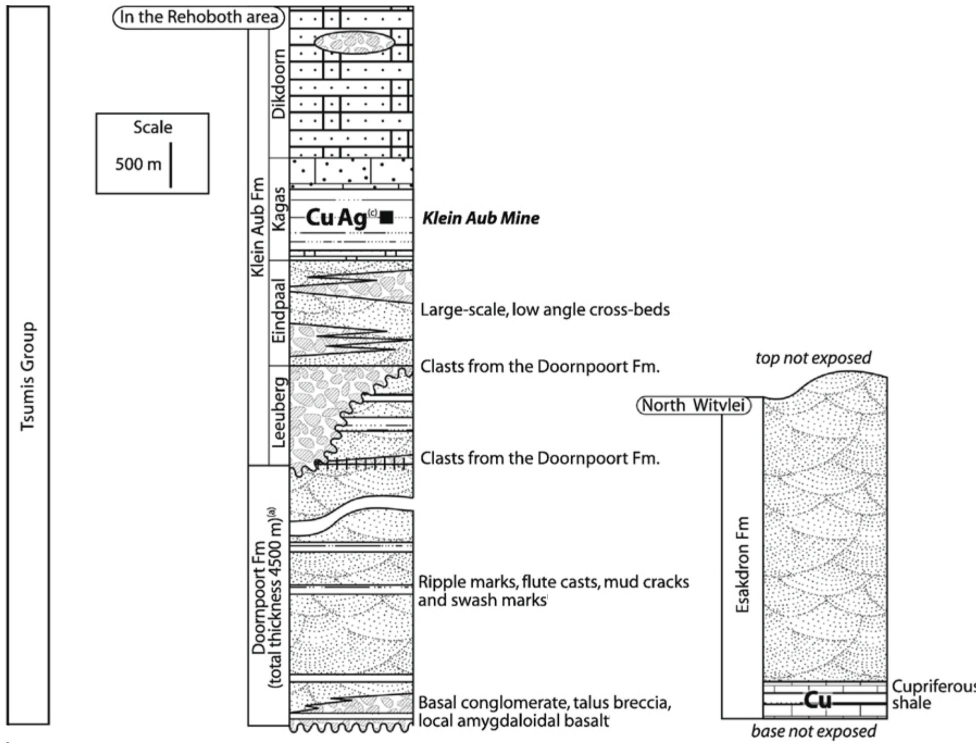

Figure 6: Stratigraphic column of the Tsumis Group. Modified from Lehmann et al., 2015.

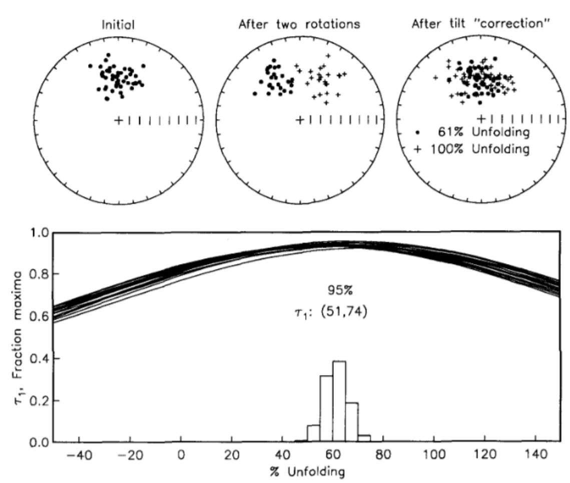

Figure 7: Example of how a vertical axis rotation can cause paleomagnetic data to appear to indicate syn-folding magnetization when the magnetization was not acquired during a folding event. "After two rotations" in figure refers to horizontal and vertical rotations. Modified from Tauxe and Watson, 1994.

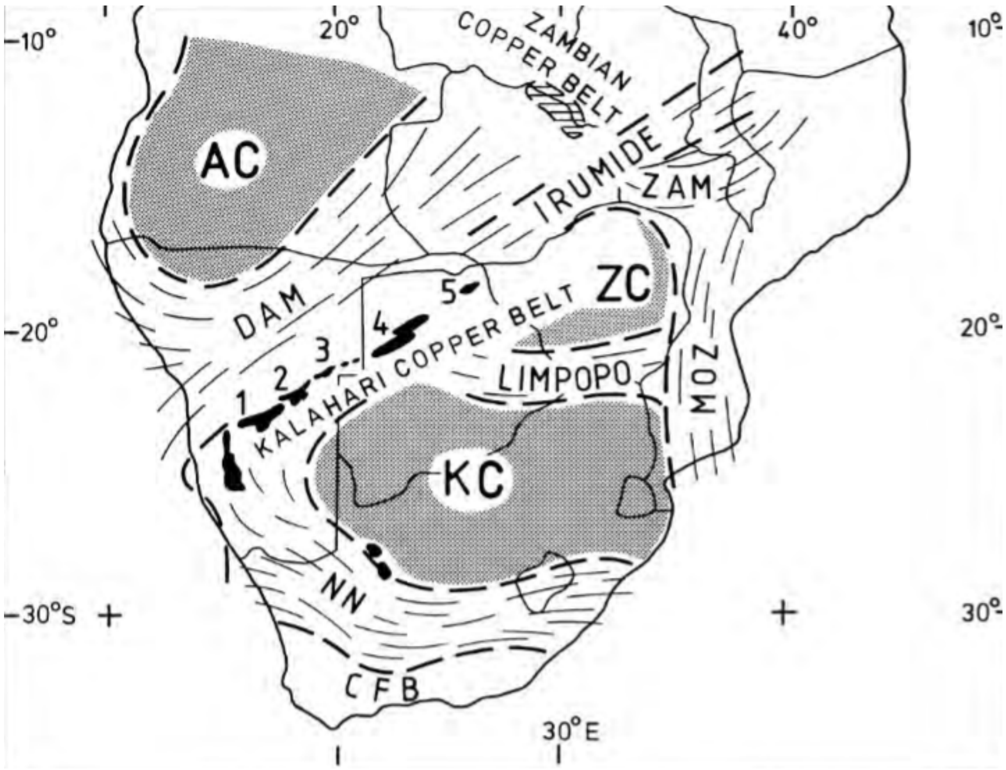

Figure 8: Map of Kalahari Copperbelt. Sampling locations approximately coincident with location 1; Eskadron Formation outcrops at 3. Modified from Borg and Maiden, 1989.

Formations. It stratigraphically post-dates the Kalahari craton's large-scale Mesoproterozoic igneous activity regardless of interpretation as Mesoproterozoic or Neoproterozoic age (Fig. 6). The Eskadron, which outcrops to the north-east of the sampling locations of this study (Fig. 8), is thought to be correlative to the Doornpoort and is differentiated in character by the occurrence of cupriferous shales and limestones at the base of the succession (Lehmann et al., 2015). It has been interpreted in the literature as deposited in alluvial fan, continental playa lake, aeolian dune, beach, and shoreface environments (Ruxton, 1986; Ruxton, 1981). The Doornpoort Formation is a thick (1,500 to 4,500 meters) red-bed clastic unit (Borg, 1987; Lehmann et al., 2015; Maiden and Borg, 2011). The Doornpoort Formation and lower members (Leeuberg and Eindpaal Members) of the Klein Aub Formation have been interpreted as deposited in small, fault-bounded intracontinental basins within braided fluvial and aeolian dune environments (e.g., Borg, 1986; Ruxton, 1986; Ruxton, 1981). Alternatively, the alluvial fan and fluvial facies of the Leeuberg and Eindpaal members have been interpreted as a progradational delta plain sequence overlying delta front marginal marine rocks of the Doornpoort Formation (e.g., Master et al., 2014). The Kagas Member of the Klein Aub, which overlies the Eindpaal, consists of quartzite, green slate, argillite, sandstone, marl, and limestone. Despite having been subjected to lower greenschist fascies metamorphism, algal mats and shrinkage cracks have been preserved as

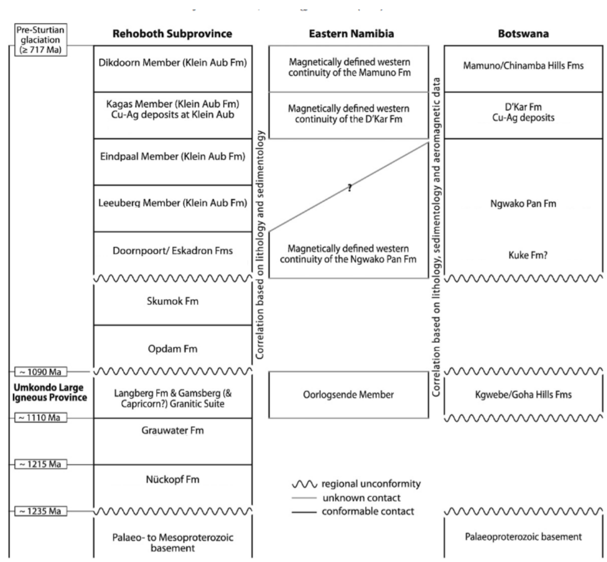

Figure 9: Stratigraphic correlations of the Kalahari Copperbelt in Naminia and Botswana.

sedimentary structures in the Klein Aub Formation. Remote sensing data suggests there may be a bedding-parallel system of thrust faults at the base of the Kagas Member (Lehmann et al., 2015; Maiden and Borg, 2011). Copper and silver deposits are hosted in beds of dark-colored dolomitic argillite (Borg, 1986). Copper genesis has been suggested to have occurred during basin inversion, metamorphism, and perhaps the very latest stages of Damara orogeny (Maiden and Borg, 2011; Sillitoe et al., 2010).

Some stratigraphic correlations suggested in the literature are available in Fig. 9.

2 Methods

2.1 Field Methods

Field sampling was carried out during July 2023 in central Namibia throughout the Doornpoort and Klein Aub formations. Samples were collected using diamond drill bits attached to gasoline-powered modified Stihl and Echo chainsaws to drill 2.54cm diameter cylindrical specimens. Samples were oriented with a Pomeroy orienting device. Structural measurements were taken using the Clino application on iPhones and iPads, an unknown application on David Evans' iPhone, and Brunton compasses.

2.2 Laboratory Methods

Thermal demagnetization and measurements were conducted at the Yale Paleomagnetic Facility using a 2G Enterprises DC-SQUID superconducting rock magnetometer. The magnetometer is housed in a magnetostatically shielded room with magnetic field magnitude of $< 1,000$ nT. It is equipped with an automated snake pick-and-place sample changing system. The samples are vacuumed up by a quartz glass sample rod and delivered to the measurement area, which typically measures at 1×10^{-9} Am^2. Prior to thermal demagnetization, samples were measured for natural remanent magnetization (NRM). Samples were then heated in an ASC Scientific Model TD-48 SC Thermal Specimen Demagnetizer for 90 minutes. Each sample was subjected to 20 to 25 heating and measuring cycles. Based on preliminary data on the Doornpoort Formation from the undergraduate work of Mai, 2021, the primary carrier of magnetization for this data set was expected to be hematite. Despite this, a cautious approach was taken and resolution of temperature step was increased moving towards the Curie temperature of magnetite (580° C, Dunlop and Özdemir, 1997), as to capture any potential magnetite component. Resolution was increased further to 5-2° C moving towards the Néel temperature of hematite (generally thought to be 680° C, Dunlop and Özdemir, 1997). Samples were heated until they no longer held stable magnetization. This occurred at up to 695° C.

2.3 Analytic Methods

Principal component analysis was conducted to determine vector components (paleomagnetic directions) using the Demag GUI portion of the PmagPy software package (Kirschvink, 1980; Tauxe et al., 2016). Statistical analysis was done in Python and made use of a combination of open source PmagPy functions and novel functions created for this study (Tauxe et al., 2016).

3 Paleomagnetic Results and Interpretation

3.1 Site-Based Data Treatment

Following principal component analysis, the data set of paleomagnetic directions underwent initial filtering in order to minimize scatter without reducing the data set significantly. Historically, paleomagnetic data has been filtered in four ways: maximum angular deviation (MAD) cut-offs, arbitrary elimination of individual outliers from site means, a k-cutoff, and enforcing a minimum number of samples n per site. Inclination shallowing was accounted for using the elongation/inclination method of Tauxe, 2005 and a flattening factor applied to compensate for the paleomagnetic phenomenon known as inclination shallowing, which causes paleomagnetic directions from clastic sedimentary rocks to appear shallower than a true reading of the Earth's magnetic field at some point in time.

3.1.1 MAD Cut-off

All vector components with a MAD greater than 15° have been excluded on grounds of being indicative of data that is highly scattered on a within-sample basis. MAD values for each vector component have been used as a reliability filter in historic and modern paleomagnetic studies with cut-off values ranging from 15° to 5° quite arbitrarily (Asefaw et al., 2021; McElhinny and McFadden, 1999). The most conservative commonly used cut-off of 15° was selected for this study, as 10° and 5° cut-offs eliminate 21% and 51% of the characteristic remanent magnetization (ChRM) components of this data set respectively. A 15° cut-off preserves 94% of the ChRM component data set. Given that MAD cut-offs have been shown to have a statistically insignificant effect on position and precision of paleopoles, a robust data set is statistically more important to paleomagnetic studies than elimination of "low quality" data (Gerritsen et al., 2022).

3.1.2 Arbitrary Elimination

A common practice in paleomagnetic studies is to apply a cut-off at the site level to remove individual outliers that lie far from the site mean (McElhinny and Merrill, 1975; Vandamme, 1994; Watkins, 1973; Wilson et al., 1972). These outliers are not thought to represent paleosecular variation of the Earth's magnetic field. Instead, they are considered to be the result of natural (e.g., lightning strikes) or human (e.g., orientation errors) phenomena. However, both a fixed 45° cut-off and a variable Vandamme cut-off have been shown to systemically underestimate inclinations in sedimentary rocks (Vaes et al., 2021). Therefore, neither a fixed-angle nor an iterative Vandamme cut-off was applied in this study.

3.1.3 k-cutoff

Paleomagnetic sites are frequently treated as representing spot readings of the paleomagnetic field at some point in time. These spot readings are expected to be Fisherian in distribution, under the assumption that scatter within a site results from randomly distributed errors (such as measuring errors) and not paleosecular variation. The Fisher, 1953 k-value is a measure of within-site precision. It measures how well a site conforms to a Fisher distribution. A low k-value indicates that the site may not be representative of a spot reading of the paleomagnetic field and should therefore be thrown out. Commonly used k-cutoff values have arbitrarily been $k = 50$ or $k = 100$ (Biggin et al., 2008; Johnson et al., 2008; Lippert et al., 2014). However, using a $k = 50$ or $k = 100$ cut-off will significantly decrease the number of sites N used to produce any paleopole (Gerritsen et al., 2022). As the cone of 95% confidence about the mean direction, A_{95}, is N dependent, decreasing N leads to an increase in the A_{95} of a paleopole. Additionally, sedimentary rocks are expected to average short-term paleosecular variation of magnetic north over the few meters a site often constitutes. Therefore, a sedimentary paleomagnetic site should not be expected to represent instantaneous spot readings of the paleomagnetic field (as igneous rocks do), instead averaging secular variation within a single site while a single site from an volcanic flow or dyke would not be expected to do so. Further, they cannot be expected to be Fisher distributed prior to correction for inclination shallowing, yet in logic that is a bit circular, inclination shallowing cannot be properly corrected for until data has been filtered (Tauxe et al., 1991). For these reasons, this study conservatively applies a k-cutoff of $k > 10$ in the style of Meert et al., 2020 in order to exclude data that is distributed near-uniformly (randomly) due to physical phenomena, such as a dominantly large magnetic particle distribution within the measured samples, but still include any potentially meaningful data (Dunlop and Özdemir, 1997).

3.1.4 Minimum Samples per Site

Various minimum number of samples per site n have been proposed. The smallest minimum n proposed for traditional site-based sampling has been three and the largest minimum n has been five (Opdyke and Channell, 1996; Tauxe, 2010). None of this study's sites have $n < 5$. No further filtering was performed.

3.1.5 E/I Method

Sedimentary rocks are prone to inclination shallowing due to ferromagnetic grains rotating during deposition and compaction, leaving detrital remanent magnetization that is biased to be shallower than a true reading of the paleomagnetic field (Tauxe, 2005). To account for this, a flattening factor should be applied. Given a large enough sample set of individual samples $n > 100-150$, a statistical method can be applied to determine

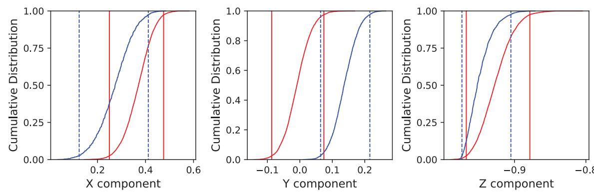

a) Bootstrap common mean test between site 23 ChRM directions and Kalfrivier-location low-temperature 'A' directions.

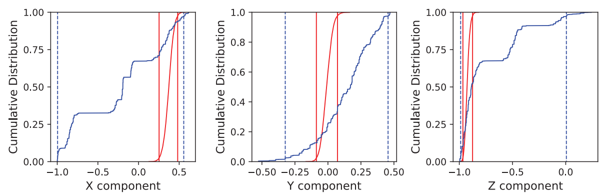

b) Bootstrap common mean test between site 25 ChRM directions and Kalfrivier-location low-temperature 'A' directions.

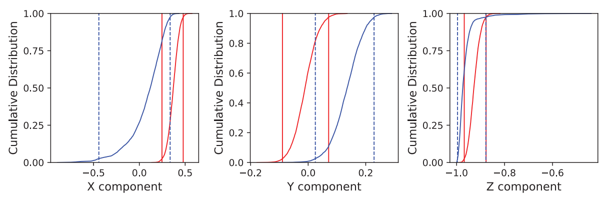

c) Bootstrap common mean test between combined site 23-site 25 ChRM directions and Kalfrivier-location low-temperature 'A' directions.

Figure 10: Bootstrap common mean test as justification for excluding sites 23 and 25 while following the Tauxe, 2005 E/I method.

the most probable flattening factor. Prior to using the elongation/inclination (E/I) method, a bootstrap common mean test and Watson common mean test were run to compare each site to the low-temperature component 'A' that agrees with the expected present local field direction (Tauxe, 2010; Watson, 1956; Fig. 10). Following elimination of two sites whose ChRM directions were found to share a common mean with the present local field (PLF), and therefore interpreted to only hold secondary magnetization, the E/I method was used to quantify a flattening factor for this data set (Tauxe, 2005). With $n = 131$ following elimination of sites 23 and 25 and a MAD cut-off of 15°, the flattening factor was found to be 0.59, a value which generally agrees with the empirical measurement of 0.61 (Pierce et al., 2022; Fig. 11). Without elimination of the two PLF sites, the flattening factor was found to be 0.75, which does not agree with empirical data. The 0.59 flattening factor was applied to the remaining data set prior to any further data analysis.

3.1.6 Summary of Data Filtering

A flattening factor of 0.59 was applied to the data set, as determined to be appropriate using the E/I method (Tauxe, 2005). This value is similar to the empirically determined value of 0.61, implying that applying a flattening factor to this data set is appropriate (Pierce et al., 2022). Following filtering data by a MAD cut-off of 15°, all sites have $n \geq 5$, so no sites were excluded on the grounds of minimum number of samples

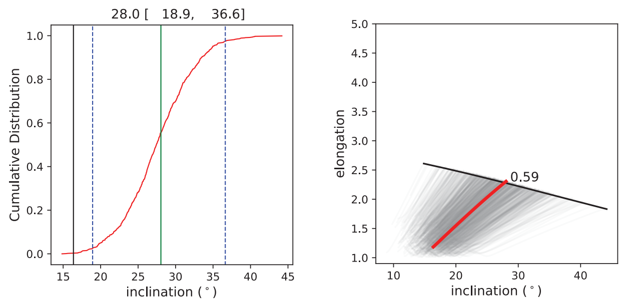

Figure 11: Results of running the Tauxe, 2005 E/I method on the non-conglomerate, non-present local field ChRM data set.

required for site-based sampling. Applying fixed-angle cut-offs or iterative Vandamme cut-offs have been shown to cause inclination to be underestimated (Vaes et al., 2021). Therefore, no fixed-angle cut-off or Vandamme cut-off was used. Sites DP2318, DP2320, DP2325, DP2326, DP2327, and DP2329 were excluded from further analysis due to $k < 10$. Site DP2323 was excluded for sharing a common mean with the low-temperature A-direction/PLF direction. The site mean data is summarized in Tbl. 1 in geographic coordinates.

3.2 Site-Level Results

Sites DP2310 through DP2330 are located along a seasonal drainage bed that is approximately parallel to the south-east younging direction of the strata, allowing sampling to be done while walking up or down the drainage (Fig. 12). The area is mapped as the Doornpoort Formation and the Leeuberg Member and Kagas Member of the Klein Aub Formation (GSN, Ministry of Mines and Energy, Sheet 2317C Tsumis Park [Provisional]). All sites are purple to purple-red to red-pink siliciclastic rocks (grain size variable from medium [generally in what is mapped as the Leeuberg Member] down to fine sand and silt, noting that there is a small window of grain size that reliably works to record paleomagnetic directions[Tauxe and Kent, 1984]). Cross bedding is prevalent throughout all sites, though efforts were made to avoid sampling in cross bedding as much as possible and take bedding measurements at the best available horizons in order to hopefully identify true paleohorizontal. Paleomagnetic results from each site are listed in stratigraphic order in Tbl. 1. Site DP2321, a conglomerate, is excluded from this section and instead discussed in Section 3.3.1. Characteristic remanent magnetization is referred to as the 'ChRM' component in the following section. Low temperature magnetization is referred to as the 'A' component.

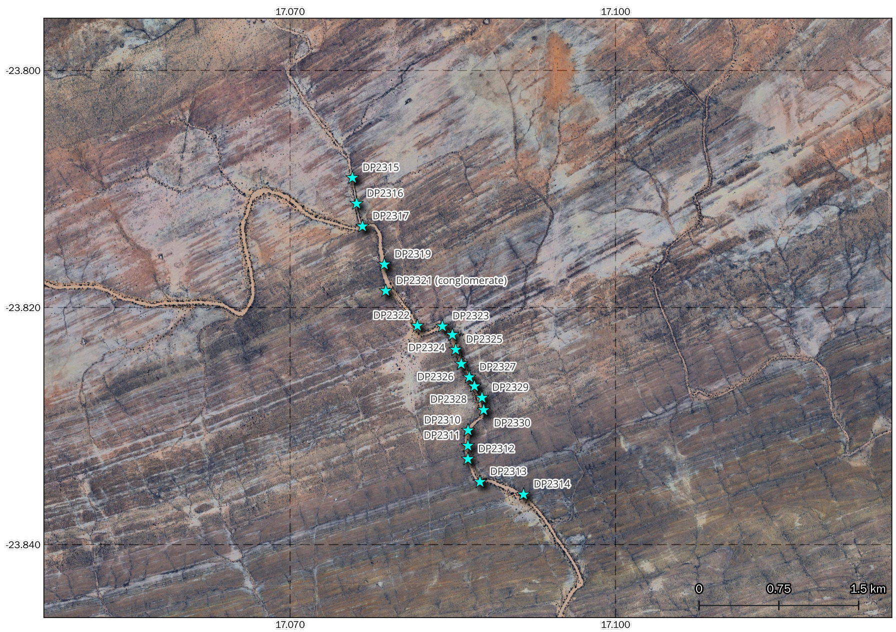

Figure 12: DP23 sampling locations.

Site Mean Data, Geographic Coordinates								
Site	Dec	Inc	n	R	k	α_{95}	csd	Plots
DP2315	186.21	21.04	8	7.96	157.81	4.42	6.45	Fig. 13
DP2316	183.80	-6.71	8	7.78	32.50	9.86	14.21	Fig. 14
DP2317	191.28	-21.50	8	7.58	16.51	14.04	19.93	Fig. 15
DP2318	199.43	-6.23	7	4.91	2.88	43.53	47.77	Fig. 16
DP2319	145.75	0.10	8	7.63	18.89	13.08	18.64	Fig. 17
DP2320	188.60	-54.48	7	6.09	6.63	25.33	31.45	Fig. 18
DP2322	198.48	-41.74	8	7.75	28.09	10.63	15.28	Fig. 19
DP2323	26.73	-72.23	7	6.83	35.46	10.28	13.60	Fig. 20
DP2324	168.46	-30.04	8	7.92	87.58	5.95	8.66	Fig. 21
DP2325	162.88	-68.10	5	2.40	1.54	180.00	65.29	Fig. 22
DP2326	218.05	-47.00	7	6.33	8.93	21.37	27.11	Fig. 23
DP2327	227.74	-49.61	6	5.36	7.78	25.63	29.03	Fig. 24
DP2328	160.29	-60.25	8	7.33	10.46	17.97	25.05	Fig. 25
DP2329	160.17	21.16	8	6.41	4.41	29.81	38.59	Fig. 26
DP2330	195.79	-21.56	8	7.37	11.05	17.43	24.36	Fig. 27
DP2310	165.43	-33.98	8	7.63	19.26	12.94	18.45	Fig. 28
DP2311	184.70	-41.52	8	7.69	22.84	11.84	16.95	Fig. 29
DP2312	165.66	-38.85	8	7.85	45.19	8.33	12.05	Fig. 30
DP2313	160.10	-13.00	8	7.34	10.55	17.88	24.94	Fig. 31
DP2314	187.58	37.09	8	7.75	27.45	10.76	15.46	Fig. 32

Table 1: Site mean data, geographic coordinates. n = number of samples after data filtering, R = resultant vector, csd = circular standard deviation. k discussed in Sec. 3.1.3.

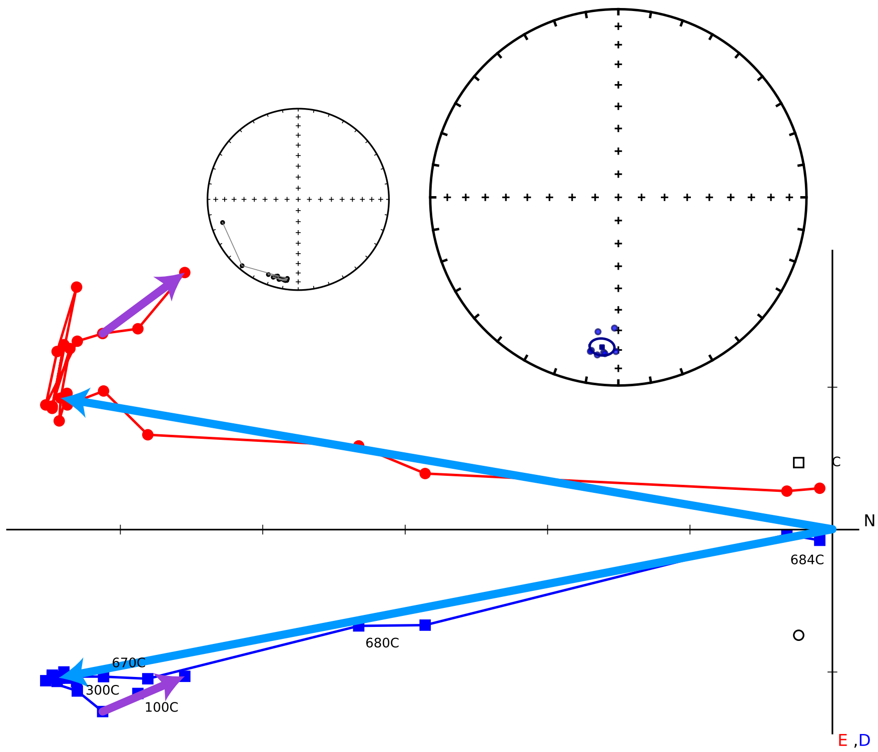

Figure 13: Site DP2315 representative thermal demagnetization data (Zijderveld diagram and small equal area plot) and site mean data (large equal area plot) in geographic coordinates.

3.2.1 DP2315

Site DP32315 consists of eight samples, none of which were excluded during data filtering. All samples displayed high-temperature decay-to-origin behavior during demagnetization, with unblocking occurring between 665-670°C as expected for hematite. All samples appeared to have a low temperature PLF component, but the low resolution of thermal demagnetization carried out at lower temperatures did not allow for the A component to be properly captured in all samples. The ChRM site mean is tightly clustered with $\alpha_{95} = 4.42$ and gives a shallow south-down direction (Fig. 13). Resultant vector $R = 7.96$, which is only slightly less than $n = 8$, further indicating tightly clustered data.

3.2.2 DP2316

Site DP32316 consists of eight samples, none of which were excluded during data filtering. All samples displayed high-temperature decay-to-origin behavior during demagnetization, with unblocking occurring between 665-670°C as expected for hematite. All samples exhibited single-component (ChRM) behavior. The ChRM site mean has an $\alpha_{95} = 9.86$ and gives a shallow south-up direction (Fig. 14).

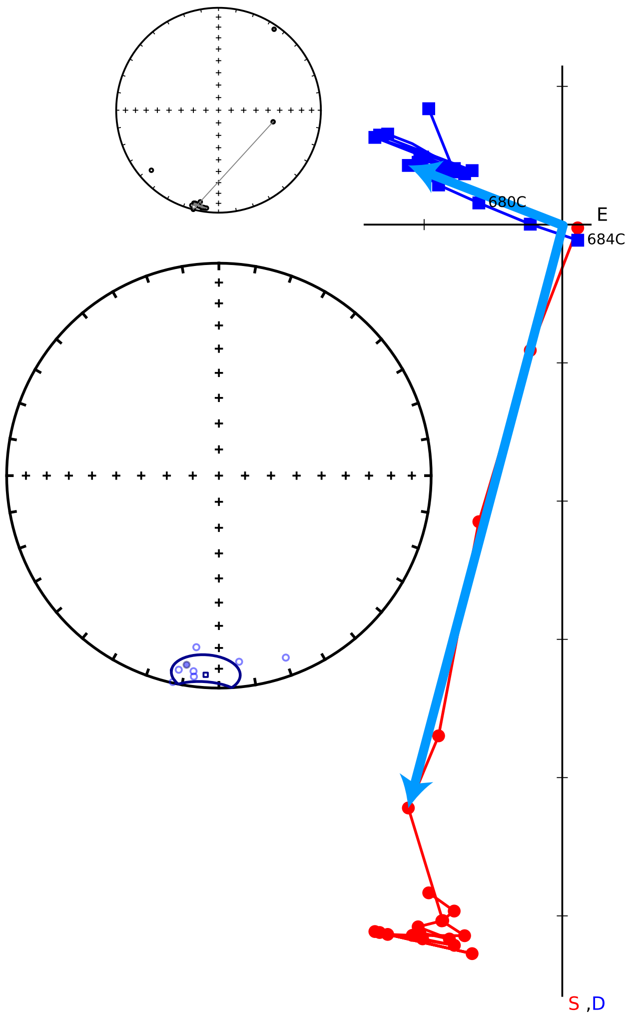

Figure 14: Site DP2316 representative thermal demagnetization data (Zijderveld diagram and small equal area plot) and site mean data (large equal area plot) in geographic coordinates.

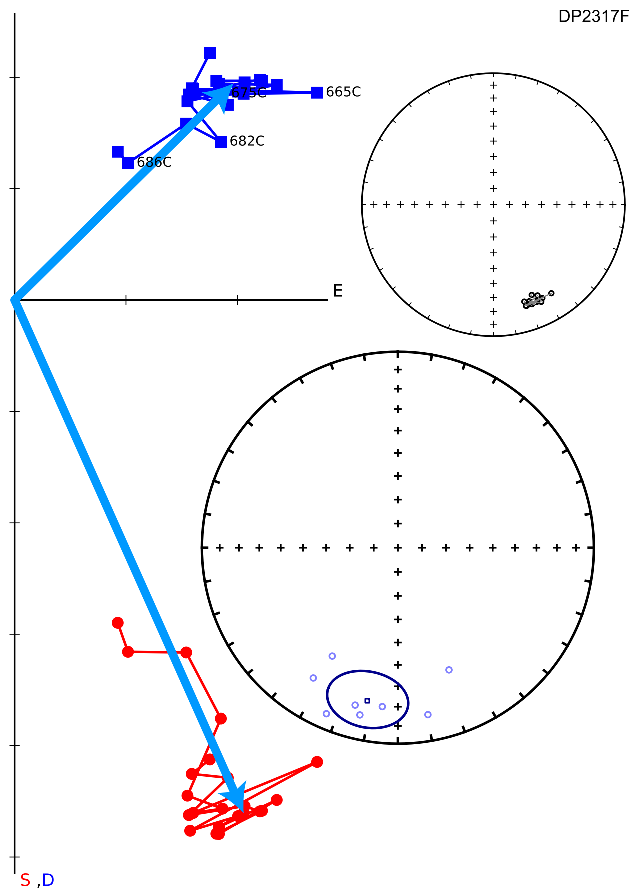

Figure 15: Site DP2317 representative thermal demagnetization data (Zijderveld diagram and small equal area plot) and site mean data (large equal area plot) in geographic coordinates.

3.2.3 DP2317

Site DP32317 consists of eight samples, none of which were excluded during data filtering. All samples displayed stable end-point behavior, with magnetization becoming unstable at >686°C and never decaying to the origin. All samples exhibited single-component (ChRM) behavior. The ChRM site mean has an $\alpha_{95} = 14.04$ and gives a shallow south-up direction (Fig. 15).

3.2.4 DP2318

Site DP2318 consisted of seven samples after data filtering, while a total of eight samples being collected in the field. All exhibited decay-to-origin behavior at high temperatures. Six samples exhibited a low-temperature PLF component. As $10 > k = 2.88$, the site was excluded from further analysis and will not be discussed further (Fig. 16).

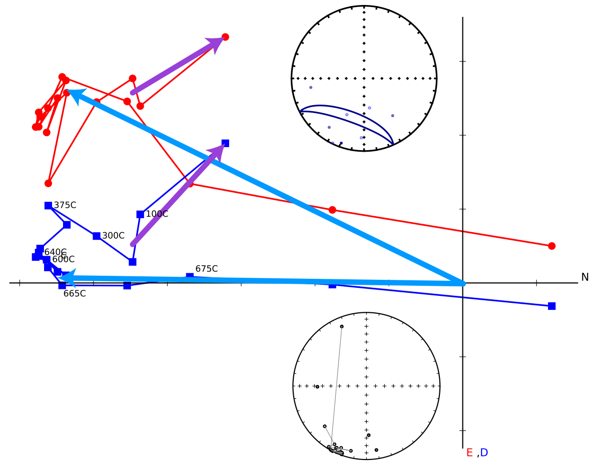

Figure 16: Site DP2318 representative thermal demagnetization data (Zijderveld diagram and equal area plot [bottom]) and site mean data (equal area plot [top]) in geographic coordinates.

3.2.5 DP2319

Site DP2319 consisted of eight samples before and after data filtering. All exhibited decay-to-origin behavior at high temperatures indicative of hematite being the primary magnetic carrier. The site mean is very shallow, southeast-up with some scatter but still over the k-cutoff of $k < 10$ (Fig. 17).

3.2.6 DP2320

Site DP2320 consisted of eight samples after data filtering. Several specimens exhibited two components and several specimens were plane-fit instead of line fit due to component mixing. As $k < 10$, this site was excluded from further analysis and will not be discussed further (Fig. 18).

3.2.7 DP2322

Site DP2322 consisted of eight samples after data filtering. All samples exhibited a PLF component and a ChRM component. All samples exhibited high-temperature decay-to-origin behavior. The site mean is south-southwest and up (Fig. 19).

3.2.8 DP2323

Site DP2323 consisted of seven samples after data filtering. Samples appeared to exhibit remarkably stable high-temperature decay-to-origin behavior that coincided with the PLF and low-temperature A-direction exhibited in other sites. While $k = 35.46$ and therefore DP2323 is not excluded on grounds of the k-cutoff, the ChRM of DP2323 was shown to share a common mean with the low-temperature A direction/PLF

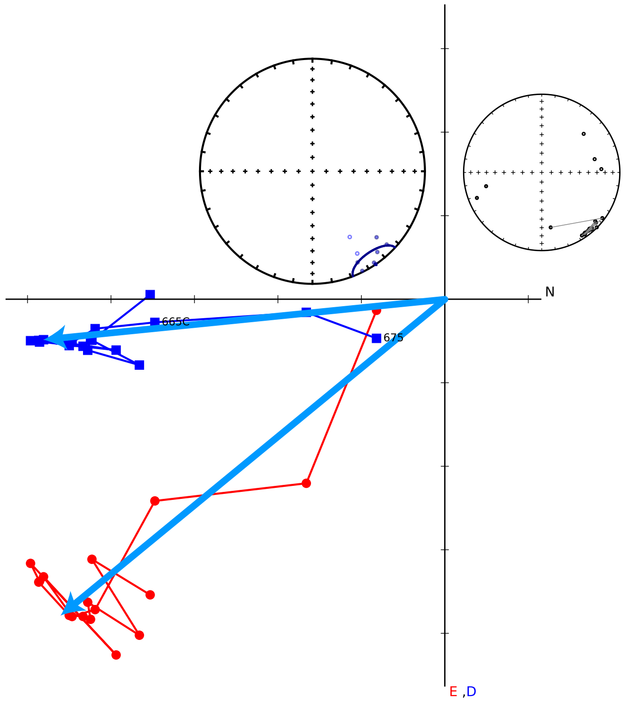

Figure 17: Site DP2319 representative thermal demagnetization data (Zijderveld diagram and small equal area plot) and site mean data (large equal area plot) in geographic coordinates.

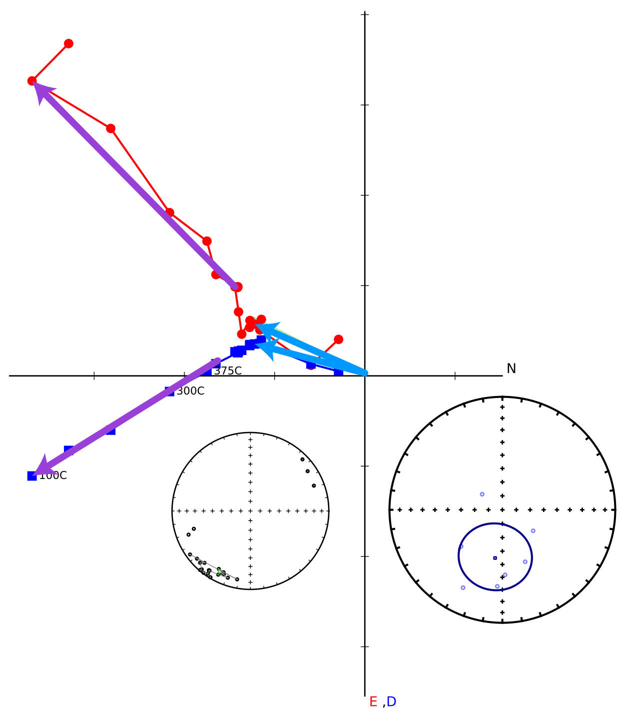

Figure 18: Site DP2320 representative thermal demagnetization data (Zijderveld diagram and small equal area plot) and site mean data (large equal area plot) in geographic coordinates.

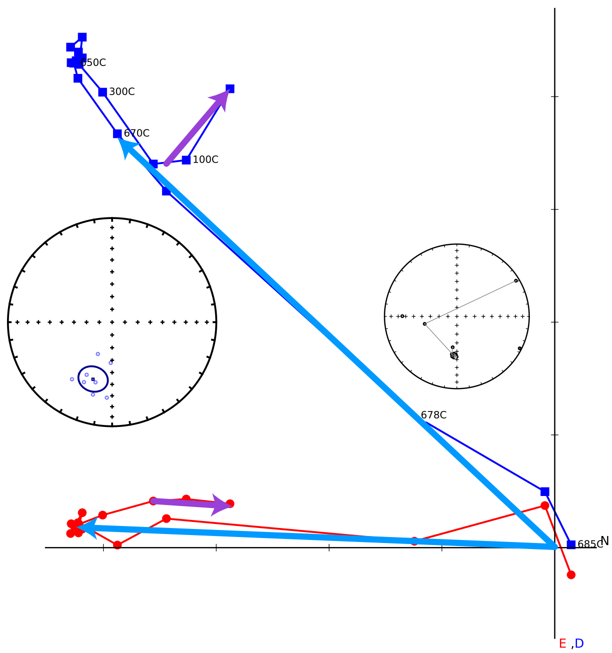

Figure 19: Site DP2322 representative thermal demagnetization data (Zijderveld diagram and small equal area plot) and site mean data (large equal area plot) in geographic coordinates.

direction. DP2323 was not included in further analysis (Fig. 20).

3.2.9 DP2324

Following data filtering, DP2324 consisted of eight samples. Site DP2324 samples exhibited the low-temperature A-component/PLF component and a high-temperature/hematite decay-to-origin ChRM component. The site mean is tightly clustered ($\alpha_{95} = 5.95$), high $k = 87.58$. The direction is south-southeast in the upper hemisphere (Fig. 21).

3.2.10 DP2325

Site DP2325 had $n = 5$ samples following data filtering. Magnetization was broadly unstable in many samples, likely because site DP2325 had the largest grain size of any sites, making the samples less than ideal for paleomagnetic study. This site was excluded from further analysis on grounds of the k-cutoff, with $k = 1.54$, indicative of near-random dispersion (Fig. 22).

3.2.11 DP2326

Site DP2326 consisted of seven samples following data filtering. Some samples displayed two components (A-component and ChRM). All samples displayed high-temperature decay-to-origin behavior. This site was

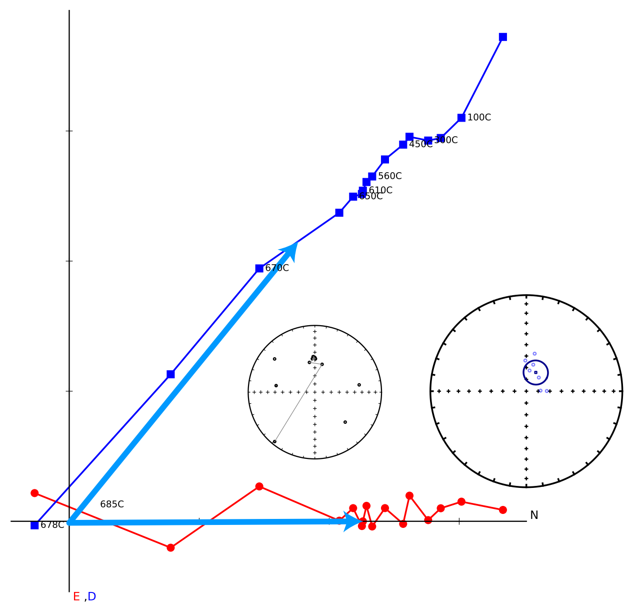

Figure 20: Site DP2323 representative thermal demagnetization data (Zijderveld diagram and small equal area plot) and site mean data (large equal area plot) in geographic coordinates.

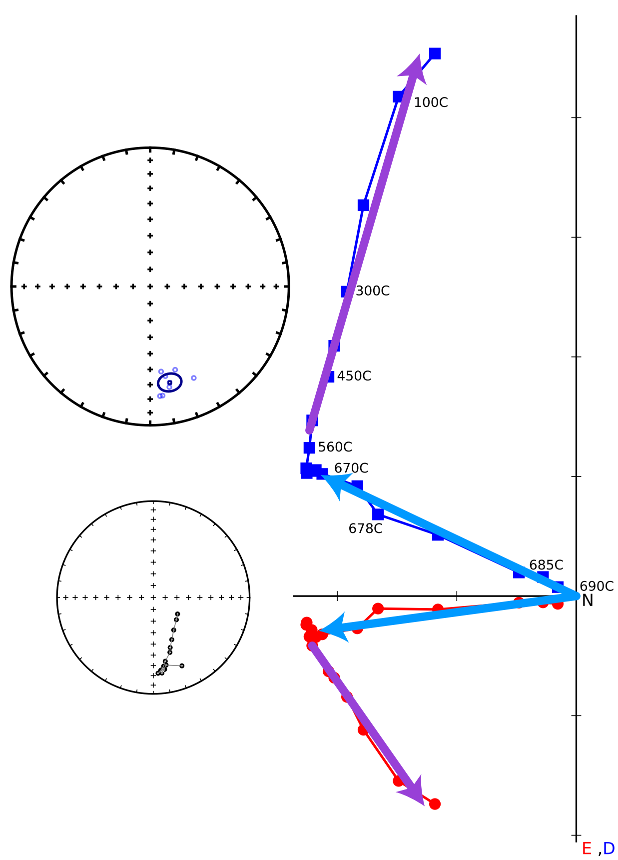

Figure 21: Site DP2324 representative thermal demagnetization data (Zijderveld diagram and small equal area plot) and site mean data (large equal area plot) in geographic coordinates.

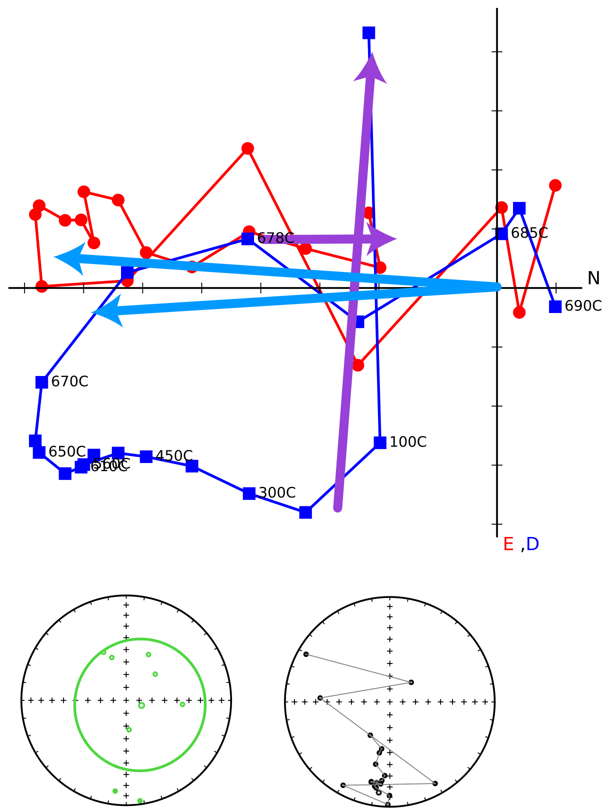

Figure 22: Site DP2325 representative thermal demagnetization data (Zijderveld diagram and equal area plot [right]) and site mean data (equal area plot [left]) in geographic coordinates.

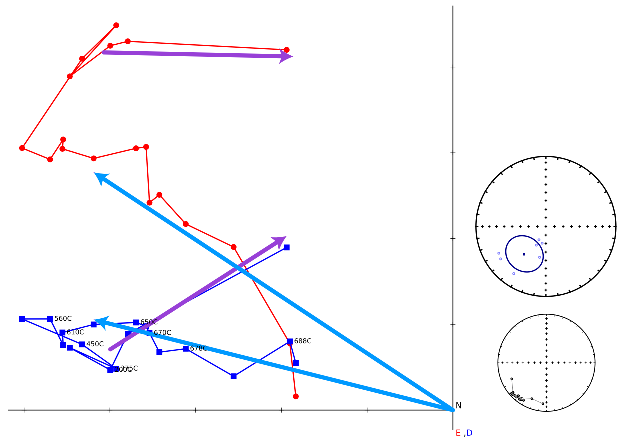

Figure 23: Site DP2326 representative thermal demagnetization data (Zijderveld diagram and small equal area plot) and site mean data (large equal area plot) in geographic coordinates.

excluded from further analysis on k-cutoff grounds (Fig. 23).

3.2.12 DP2327

Site DP2327 consisted of six samples following data filtering. Unfortunately, the likely true ChRM component was unable to be isolated in the majority of the samples due to the oven drifting in temperature from 683°C to 688°C - a critical temperature step. Ideally, this site would have been heated from 681°C to 683°C to 685°C, etc, until the magnetization decayed to the origin. The best example of the likely true ChRM component is shown in Fig. 24, though this example likely suffered from component mixing and the true ChRM may not have been fully isolated. Most of the samples from this site suffered from severe component mixing and ChRM line fits are likely not representative of the true ChRM direction. Regardless, the data available leaves this site with $k = 7.78$. This site was not analyzed further on the grounds of the k-cutoff value.

3.2.13 DP2328

Site DP2328 often had two components - a low-temperature A component and the ChRM components. This site had eight samples prior to and following data filtering. All displayed hematite-like demagnetization behavior. The site mean is south-southeast up and steep (Fig. 25).

3.2.14 DP2329

Site DP2329 displayed significant amounts of variability between samples within the site. Some samples had two components. This site had eight samples prior to and following data filtering. The site mean is southeast

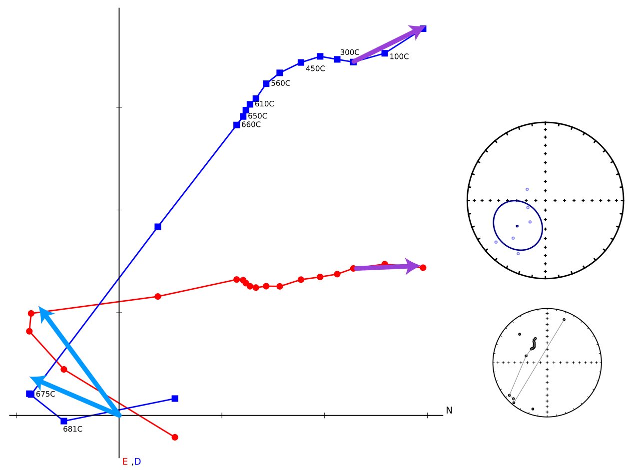

Figure 24: Site DP2327 representative thermal demagnetization data (Zijderveld diagram and small equal area plot) and site mean data (large equal area plot) in geographic coordinates.

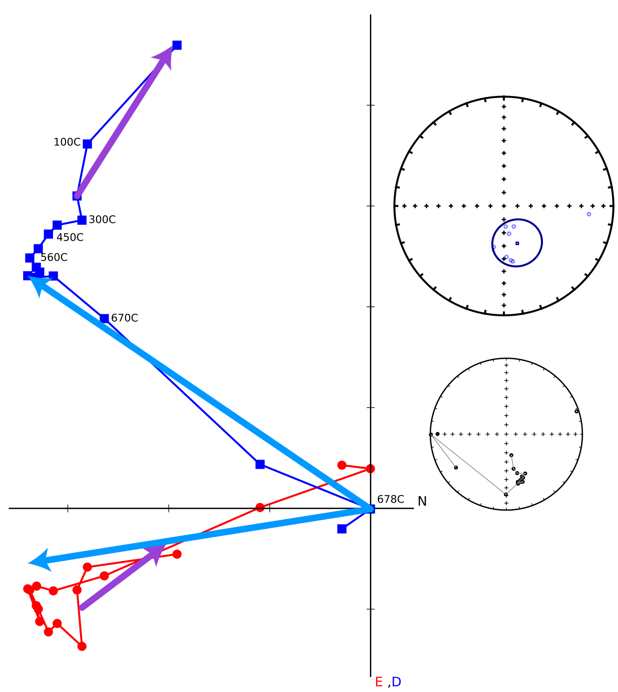

Figure 25: Site DP2328 representative thermal demagnetization data (Zijderveld diagram and small equal area plot) and site mean data (large equal area plot) in geographic coordinates.

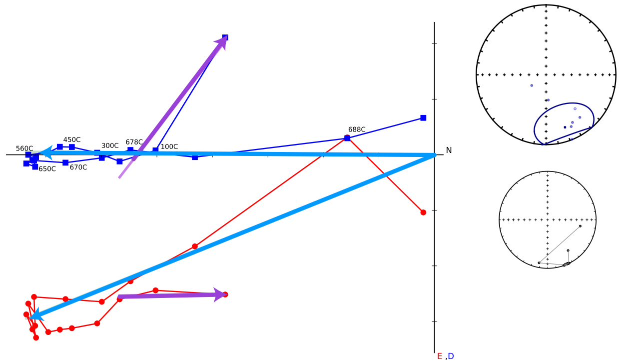

Figure 26: Site DP2329 representative thermal demagnetization data (Zijderveld diagram and small equal area plot) and site mean data (large equal area plot) in geographic coordinates.

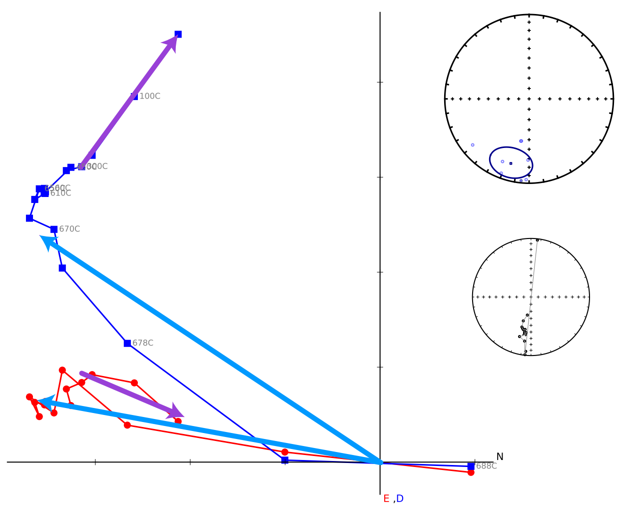

Figure 27: Site DP2330 representative thermal demagnetization data (Zijderveld diagram and small equal area plot) and site mean data (large equal area plot) in geographic coordinates.

shallow up. (Fig. 26).

3.2.15 DP2330

Site DP2330 displayed significant amounts of variability between samples within the site. Some samples had two components. This site had eight samples prior to and following data filtering. The site mean is southwest shallow up. (Fig. 27).

3.2.16 DP2310

Site DP2310 samples frequently had two components and displayed component mixing, with the ChRM component only becoming apparent at the highest temperature steps following a period of semi-stable end-point behavior. This site had eight samples prior to and following data filtering. Some samples had two

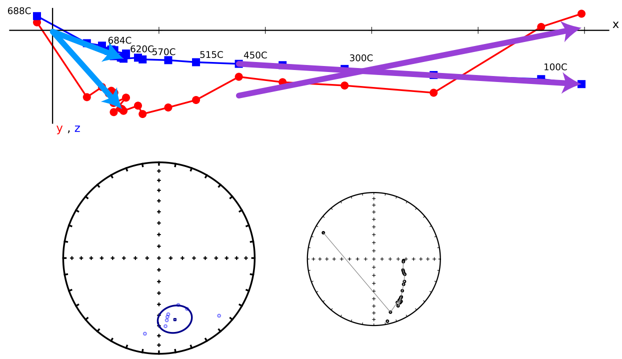

Figure 28: Site DP2310 representative thermal demagnetization data (Zijderveld diagram and small equal area plot) and site mean data (large equal area plot) in geographic coordinates.

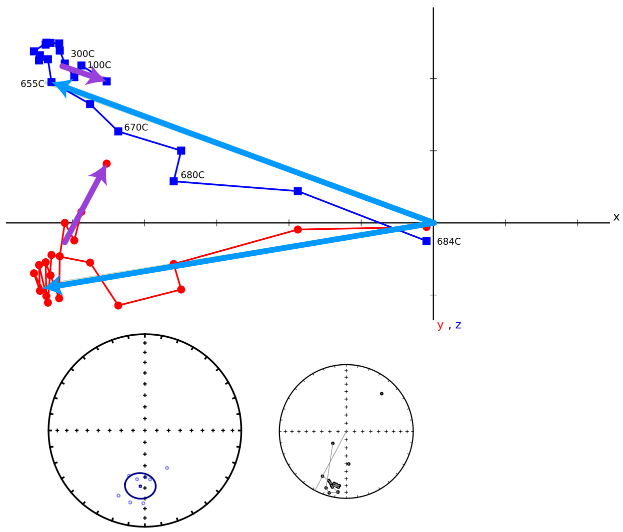

Figure 29: Site DP2311 representative thermal demagnetization data (Zijderveld diagram and small equal area plot) and site mean data (large equal area plot) in geographic coordinates.

components. The site mean is southeast shallow up (Fig. 28).

3.2.17 DP2311

Site DP2311 samples frequently had two components. Like DP2311, they sometimes displayed component mixing, with the ChRM component only becoming apparent at the highest temperature steps following a period of semi-stable endpoint behavior. This site had eight samples prior to and following data filtering. The site mean is south-southwest up (Fig. 29).

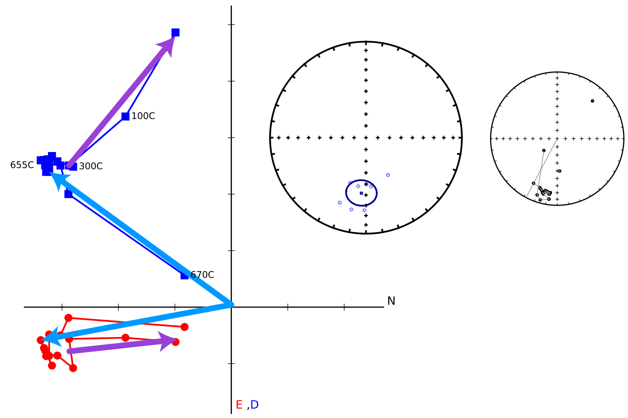

Figure 30: Site DP2312 representative thermal demagnetization data (Zijderveld diagram and small equal area plot) and site mean data (large equal area plot) in geographic coordinates.

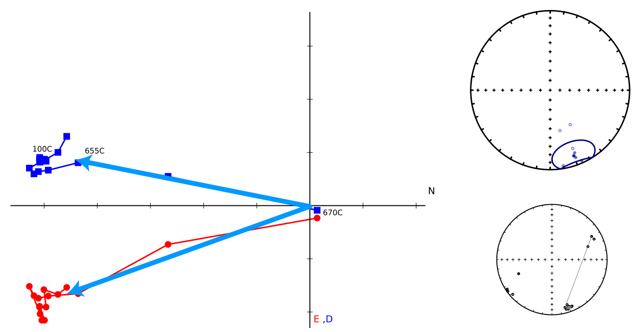

Figure 31: Site DP2313 representative thermal demagnetization data (Zijderveld diagram and small equal area plot) and site mean data (large equal area plot) in geographic coordinates.

3.2.18 DP2312

Site DP2312 samples displayed two distinct components. This site had eight samples prior to and following data filtering. The lowest temperature steps gave a PLF component. Samples then generally settled into a stable end point and fully demagnetized to the origin by 670-680° (Fig. 30).

3.2.19 DP2313

Site DP2313 samples were generally very well-behaved, displaying stable-end points and heading to the origin at the highest temperatures. This site had eight samples prior to and following data filtering. Despite this, the site still has a large amount of scatter. The site mean direction is southeast, shallow and up (Fig. 31).

3.2.20 DP2314

Site DP2314 samples all have stable end points and then decay to the origin in the one or two highest temperature steps. This site had eight samples prior to and following data filtering. This site is tightly

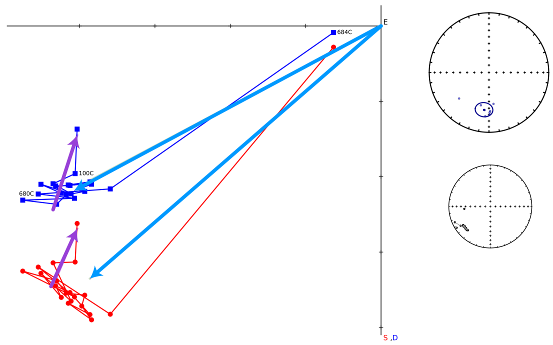

Figure 32: Site DP2314 representative thermal demagnetization data (Zijderveld diagram and small equal area plot) and site mean data (large equal area plot) in geographic coordinates.

grouped. The site mean direction is south and down (Fig. 32).

3.3 Field Stability Tests

For paleomagnetic data to be useful in the task of reconstructing paleogeography, it is best if the acquisition of paleomagnetic vector components can be constrained in age relative to geologic events (e.g., the folding that occurs during orogenies) due to the issue of potential remagnetization or "overprint". Remagnetization of sedimentary rocks is a widespread issue (McCabe and Elmore, 1989). The presence of remagnetization can partially or completely obscure the magnetization that is "primary", i.e., the magnetization that was acquired during deposition, or close enough in time (generally $<\sim$ 15 million years) to deposition such that its post-depositional nature is immaterial for the purpose of a paleomagnetic study interested in producing a paleomagnetic pole used in an apparent polar wander path, assuming normal behavior (e.g., dipolar and void of numerous rapid reversals in short succession) of the Earth's magnetic field (Meert et al., 2020).

This study is particularly concerned with remagnetization via viscous remanent magnetization (VRM), thermoviscous remanent magnetization (TVRM), and chemical remanent magnetization (CRM). Natural VRM is acquired from exposure to the Earth's magnetic field over time. With more time, more grains will have the thermal energy required to align their magnetizations with the present-day local field (Tauxe, 2010). Often, VRM can be isolated during thermal demagnetization at low temperatures (Butler, 2004). TVRM is similar to VRM. However, TVRM occurs in conjunction with exposure to heat that is below Curie and Néel temperatures but increased from Earth surface temperatures. In turn, the higher temperatures at which TVRM occur causes TVRM to occur on a shorter timescale than VRM due to more available activation energy (Yu and Tauxe, 2006). Rocks that have been deeply buried are particularly susceptible to TVRM overprint (Kent, 1985; Kent and Miller, 1987). CRM in sedimentary rocks occurs in the presence of post-detrital magnetic mineral formation. This often occurs directly (geologically speaking) before, during, and/or after orogenesis due to fluid flow, which can be illustratively described as 'squeegee tectonics' (Oliver, 1986; McCabe and Elmore, 1989; Stamatakos et al., 1996).

One tool in disentangling the primary detrital remanent magnetization (DRM) and any secondary remagnetization of sedimentary rocks is the suite of paleomagnetic field stability tests. Field stability tests are used to constrain the acquisition of magnetization relative to geologic events of known ages. Of particular importance in paleomagnetic studies of sedimentary rocks are intraformational conglomerate tests and regional fold tests (Fig. 33, 34; Graham, 1949).

3.3.1 Eindpaal Member Conglomerate Test

Conglomerate tests, at their most basic, rely on simple logic: if the magnetization of conglomerate clasts was acquired prior to deposition, then the paleomagnetic vectors of the clasts should be oriented randomly

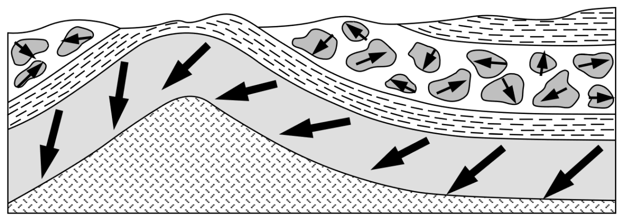

Figure 33: Schematic of ‘positive’ conglomerate and fold (bedding-tilt) tests. From Butler, 2004.

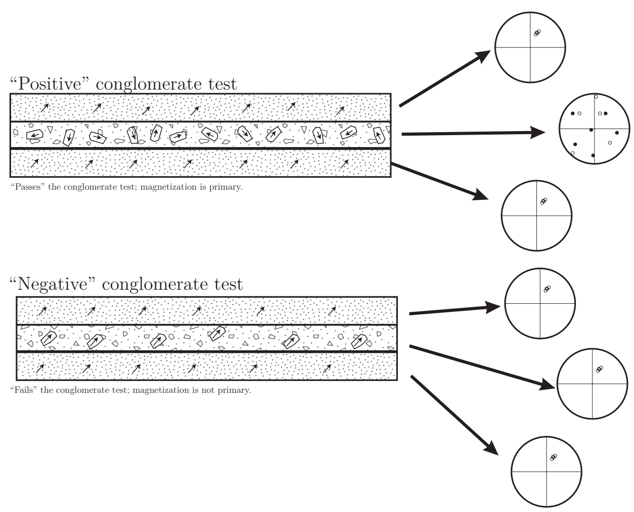

Figure 34: ‘Positive’ and ‘negative’ conglomerate tests. Modified from Meert et al., 2020.

- that is, in a uniform distribution (Fig. 34). Using the test to constrain the magnetization as "primary" relies on two assumptions; first, that the clasts themselves were randomly oriented at deposition and second, that some portion of magnetization of the clasts has been stable in the time between erosion from the host rocks and measurement in a laboratory. A conglomerate test is "positive" if the ChRM directions indicate that the host rocks have not suffered pervasive remagnetization and "negative" if the directions indicate that they have.

The earliest conglomerate tests relied on interpretive methods or "look tests" (Fisher, 1953; Graham, 1949). Early conglomerate tests were also limited in usefulness due to potential contamination by a component or components of non-primary magnetization; the advent of principal component analysis reduced but did not eliminate this risk (Kirschvink, 1980; Starkey and Palmer, 1971). Further iterations of conglomerate tests introduced statistical tests for uniformity using different mathematical methods, all of which have comparable sensitivities (Fisher et al., 1993; Mardia, 1975; Watson, 1956). More recent, improved versions take slightly different approaches. The conglomerate test used in this study statistically tests for a uniform distribution while also testing for an expected direction within the uniform distribution (Shipunov et al., 1998); an option for future analysis is the Bayesian approach (Heslop and Roberts, 2018). Here, we use the equation:

$$\rho = \frac{1}{n} \sum \cos \ \varphi_i$$

where n is the sample size, φ_i is the angle between the i^{th} unit vector and the unit vector of the expected direction, and ρ represents number that can be compared to the n dependent 95% critical value and interpreted as the conglomerate test "passing" or "failing".

Ten versions of the Shipunov conglomerate test were performed (Tbl. 3, Tbl.2). The first set of tests use the direction of the present local field (PLF) as the expected direction. The second set of tests use the direction that is given by the overlying and underlying sediments of this study as the expected direction (referred to here as the ChRM direction) in an effort to test the expected "primary" direction as a direction that is not, in fact, primary. Of 26 total samples, this conglomerate test contains 22 samples from 11 clasts. A portion of samples from the same clast give directions that are internally inconsistent to varying degrees (Fig. 35). To deal with this issue, arbitrary cut-offs of 35°, 30°, 25°, 20° and 15° degrees of internal consistency were introduced to the tests for each expected direction (Fig. 36).

For completeness' sake, the Watson (1956) conglomerate test was performed on all arbitrary cut-offs. All Watson tests were positive; however, the Watson test is significantly less meaningful than the Shipunov test and therefore the results were not interpreted as reliable for this study.

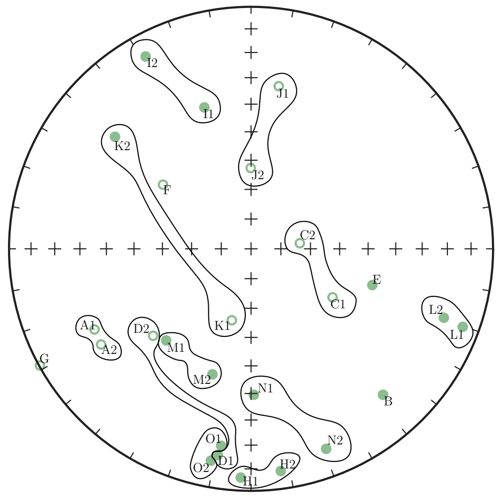

Figure 35: Conglomerate test equal area plot, prior to any data filtering.

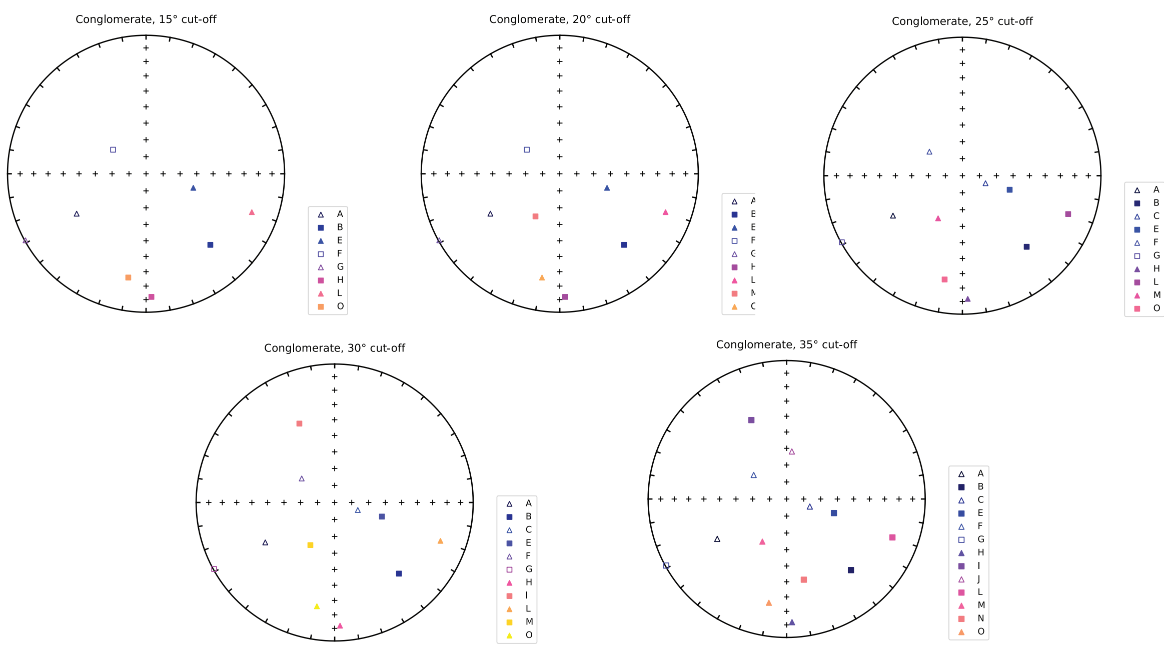

Figure 36: Equal area plots of the conglomerate test site with varying cut-offs.

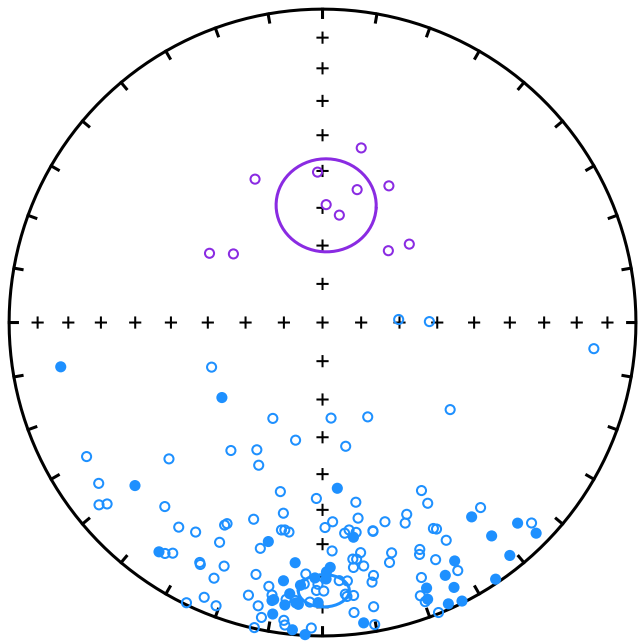

Figure 37: ChRM mean (bottom) that the conglomerate test data was tested against in the Shipunov tests and common mean tests.

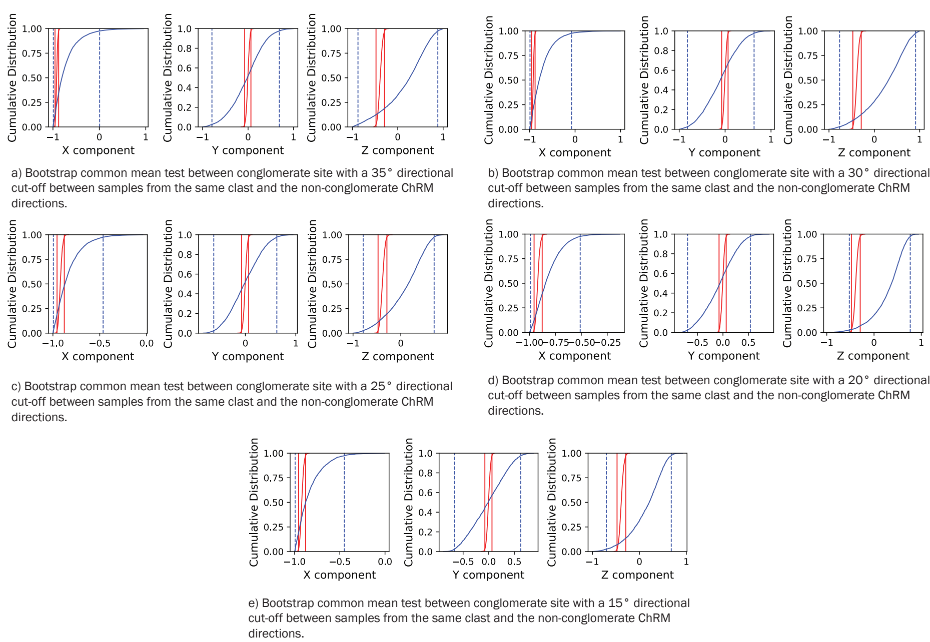

Figure 38: Bootstrap common mean tests between non-conglomerate, non-PLF ChRM directions and conglomerate clast directions with varying same-clast angular cut-offs. All show a shared common mean (via the red data overlapping with the blue data), indicative of shared magnetization between the conglomerate test and ChRM directions and hinting at shared non-primary magnetization.

Conglomerate Tests		
Cut-off Angle	Shipunov (PLF)	Watson
35°	Positive	Positive
30°	Positive	Positive
25°	Positive	Positive
20°	Positive	Positive
15°	Positive	Positive

Table 2: Shipunov conglomerate test (expected direction of the present local field) and Watson conglomerate test.

Conglomerate and Common Mean Tests		
Cut-off Angle	Shipunov (ChRM)	Bootstrap Common Mean (ChRM)
35°	Positive	Shares common mean
30°	Positive	Shares common mean
25°	Negative	Shares common mean
20°	Negative	Shares common mean
15°	Negative	Shares common mean

Table 3: Shipunov conglomerate test (with an expected direction of the non-conglomerate ChRM directions) and common mean test data of the conglomerate test against the ChRM directions.

All Shipunov conglomerate tests were positive when the expected direction used was the present local field direction. However, three of the five Shipunov conglomerate tests performed against the ChRM direction of this study were negative. These three were the tests that had the highest standard for an angle between samples from the same clast - the most demanding of the tests with respect to internal consistency of clasts. Given this result, all the cut-off angle data sets were compared to the ChRM directions in a bootstrap common mean test. Every bootstrap common mean test passed; that is to say, regardless of the cut-off angle between samples from the same clast, the conglomerate site was shown to share a common mean with the ChRM directions of the strata that lies above and below the conglomerate unit.

3.3.2 Tsumis Group Fold Test

Fold tests are commonly invoked in paleomagnetic studies as a way to constrain the age of magnetization to having been acquired before, during, or after the folding that occurs during orogenic events (Graham, 1949). If magnetization was acquired before the folding (or tilting), then the paleomagnetic directions will be best grouped when tilt-corrected. Conversely, if magnetization was acquired after the folding, then the paleomagnetic directions will be best grouped in geographic coordinates (Fig. 39). If magnetization was acquired during folding, then the data will be best grouped between 0% and 100% unfolding - though such a situation does not necessarily imply that the magnetization was acquired at the time of folding as structural complications (such as rotations about multiple axes) can contaminate fold tests in such a way

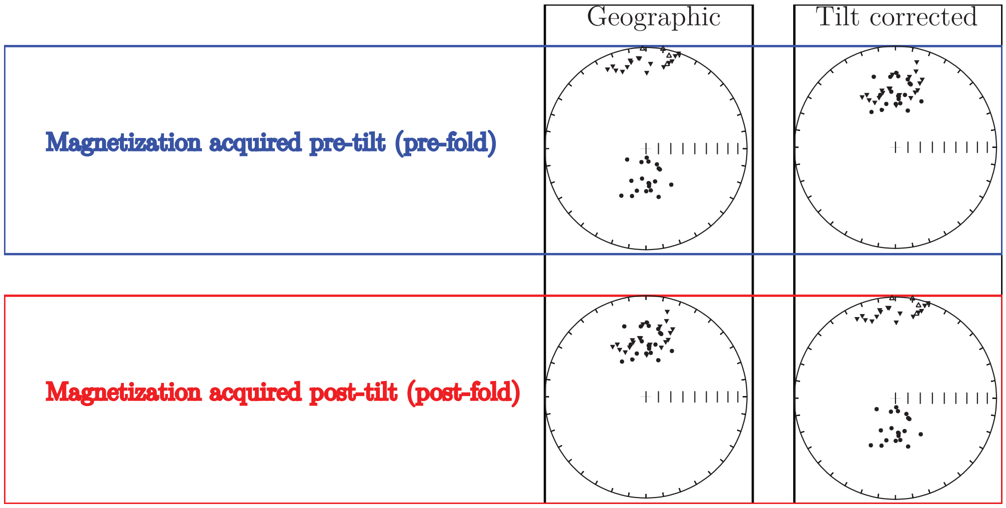

Figure 39: Paleomagnetic directions on a stereonet showing pre-tilt and post-tilt magnetization. Modified from Tauxe, 2010.

that magnetization appears to have been acquired during folding when it was not (Tauxe and Watson, 1994).

Unpublished preliminary data potentially implies syn-folding acquisition of magnetization for the Doornpoort Formation due to best clustering at 60% unfolding using the incremental fold test (Mai, 2021; Fig 40). As a parametric bootstrap approach at the sample level is the more statistically robust method, the fold test of Mai, 2021 was redone using this method (Fig. 41). It exhibits a similar syn-folding result to the incremental fold test of Mai, 2021 but instead shows best clustering at 62-78% unfolding.

On the basis of the Doornpoort fold test of Mai, 2021, the Doornpoort and Klein Aub formations of the Tsumis Group were sampled for a fold test in this study. A parametric bootstrap fold test was performed at the site-mean level and the more statistically robust sample level. Neither approach exhibits behavior similar to the incremental fold test of Mai, 2021 or parametric bootstrap fold test using the same data; instead, a fold test at the site level is indeterminate and a fold test at the sample level is negative (Figs. 42, 43). However, when only samples that are mapped as the Kagas Member of the Klein Aub Formation are run in a bootstrap fold test, the result instead becomes indeterminate (Fig. 44). Kagas Member sites are interpreted to be DP2329, DP2330, DP2310, DP2311, DP2312, DP2313, and DP2314. When samples mapped as Doornpoort, interpreted to be sites DP2315, DP2316, DP2317, DP2318, and DP2319, are run in a bootstrap fold test, they fail which can be interpreted as magnetization having been acquired after folding. However, when combined and the Leeuberg member samples excluded, the Doornpoort and Kagas samples are indeterminate (Fig. 57).

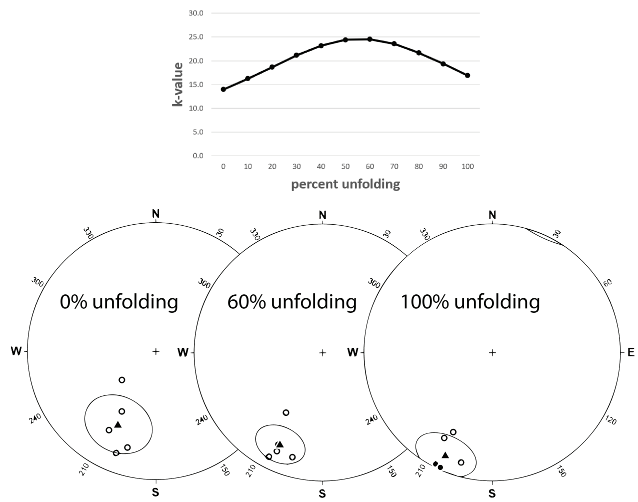

Figure 40: Potentially syn-folding incremental fold test from preliminary data of Mai, 2021. Modified from Mai, 2021.

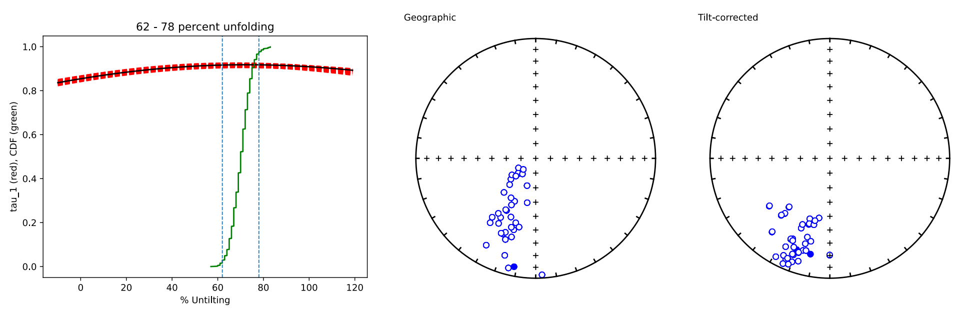

Figure 41: Potentially syn-folding parametric bootstrap fold test using sample-level data from Mai, 2021. Behavior when run at the site-level is as similarly inconclusive as Fig. 42 due to the low number of sites not allowing for meaningful statistical inferences to be made.

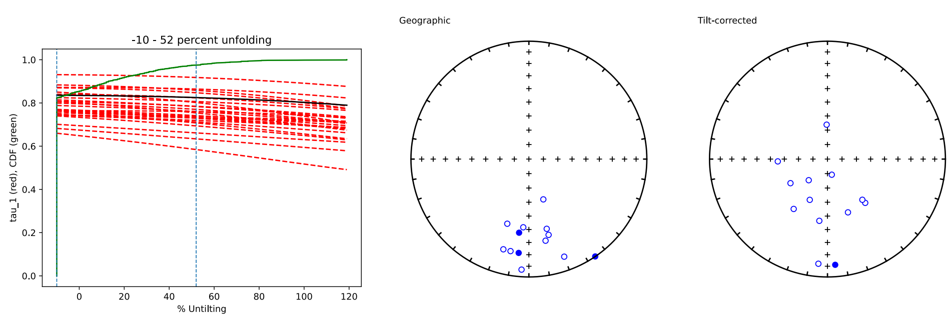

Figure 42: Statistically indeterminate parametric bootstrap fold test using site-mean level data from this study.

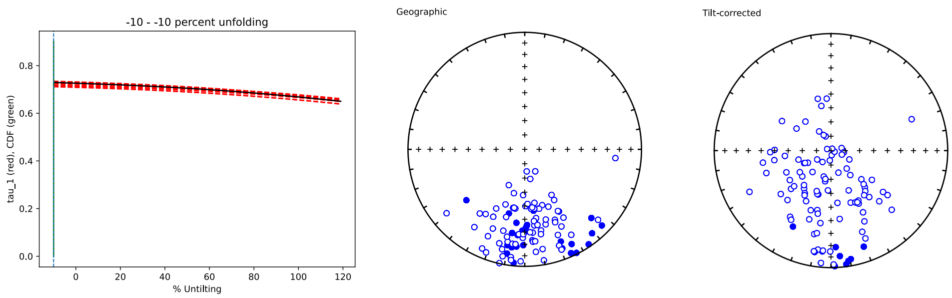

Figure 43: Negative parametric bootstrap fold test using sample-level data from this study.

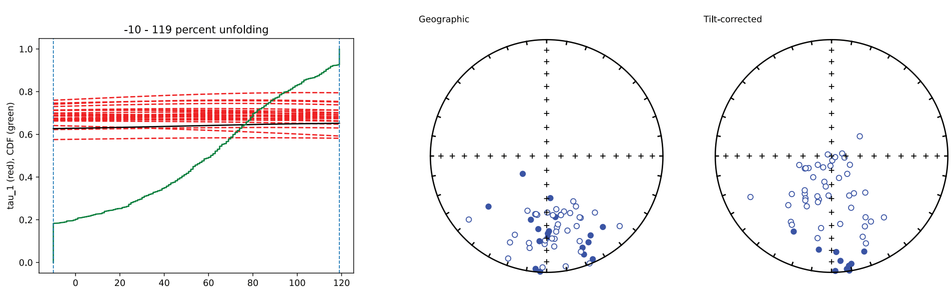

Figure 44: Indeterminate parametric bootstrap fold test using sample-level Kagas Member data from this study.

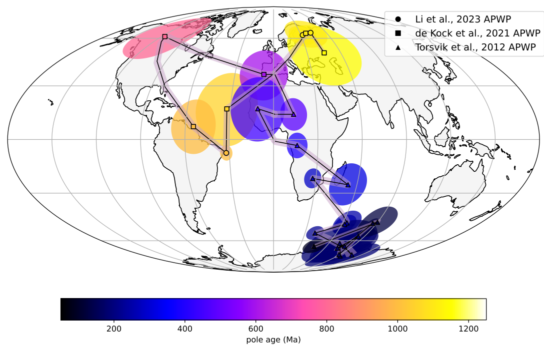

Figure 45: Compiled apparent polar wander paths from de Kock et al., 2021; Li et al., 2023; Torsvik et al., 2012. Note that de Kock et al., 2021's path has been smoothed, and $\leq$ 800 Ma de Kock poles have arbitrarily been assigned $\alpha_{95} = 15$ as no α_{95} is available.

4 Discussion

While there are no published "A"-grade poles from approximately 1000 Ma to 500 Ma for the Kalahari craton, non-"A"-grade poles were compiled and smoothed in de Kock et al., 2021, and have been included in Fig. 45 in tandem with the poles used in the reconstructions of Li et al., 2023 and Torsvik et al., 2012. This figure is displayed for the reader (and also the author, who was at various points during the process of putting together this thesis was extremely annoyed at the lack of an up-to-date combined Precambrian and Phanerozoic Kalahari APWP figure in the literature) as a reference of a whole-Earth apparent polar wander path for the Kalahari craton. It was compiled from a variety of sources in an attempt to limit any bias the various authors may have when selecting paleomagnetic poles for their models.

For the sake of calculating poles, this study treats each sample as its own "site", in the style of magnetostratigraphy. Generally, site-based grouping is used to connect samples believed to be of a similar age together over a large area (i.e., dyke swarm sites). All the sites included in this study are from within 3.5 kilometers of each other and the stratigraphic order of the sites is known. While the sampling was carried out in a site-based style, the author believes that treating this study as a magnetostratigraphic data set is appropriate and may be more meaningful than treating groupings of samples as sites. Therefore, each sample was treated as its own site and assigned its own virtual geomagnetic pole (VGP) prior to computing the aggregated poles discussed below.

There are lines of evidence to suggest that the magnetization of the samples presented in this study is both primary (i.e., acquired at deposition or shortly thereafter) and secondary (i.e., acquired after folding). The Shipunov conglomerate test at $\leq 25°$ is interpreted to support magnetization that is post-deposition. However, as the number of clasts present in a conglomerate test decreases, so does the usefulness of the test. Conversely, the Watson conglomerate test and Shipunov conglomerate test at $\geq 30°$ support magnetization that is coincident with when these rocks were deposited, and most paleomagnetic studies would take a Watson conglomerate test at face value. Similarly, the fold tests could be interpreted conservatively as post-folding magnetization or as being meaningless entirely. Even when the fold tests fail, they do not do so in a spectacular fashion, and could instead be pushed to pass by bedding measurements that are a few degrees different. Given the cross-bedding that is prevalent throughout the section and the difficulty in attaining bedding measurements that definitively represent paleohorizontal, it is certainly possible that the fold tests were subtly compromised. Additionally, these fold tests do not draw from opposing limbs of a fold - instead, bedding measurements are relatively (though not completely) similar throughout the section. Perhaps most notably, the data has been numerically determined to be in need of a flattening factor $f = 0.59$, despite basic logic suggesting that data from overprinted clastic sedimentary rocks would not be distributed in such a way. Magnetization has been interpreted in the literature as primary with evidence similar to that which is presented in this study (e.g, the thrown out Shipunov conglomerate test of de Kock et al., 2009).

However, the data presented in this study does not behave in a nature similar to the preliminary Doornpoort paleomagnetic study of Mai, 2021, which was interpreted as syn-folding magnetization. Correct structural reconstructions using syn-folding magnetizations are difficult to ascertain and true syn-folding magnetization is difficult to show. If beds have been rotated about multiple axes (such as a vertical axis and a horizontal one), then a clustering peak can occur that implies syn-folding magnetization when instead structural complications are causing the “syn-folding” peak (Tauxe and Watson, 1994). To further complicate matters, the syn-folding magnetization that is implied from the incremental fold test employed in the preliminary work of Mai, 2021 is based on an assumption of folding that is proportional at each limb. This assumption has been shown to not always be true (Cairanne et al., 2002; Delaunay et al., 2002; Suppe, 1983; Villalaín et al., 2003).

Mai, 2021 and Chung-Halpern, 2021 proposed that the Rehoboth Basement Inlier rotated 25-30° as its own microcontinental block at ca. 500 Ma and the Doornpoort post-folding pole of Piper, 1975 is interpreted as Damara-era overprint (Fig. 46). Those studies also proposed that a previously unidentified ca. 1100 Ma folding event occurred within the Rehoboth Basement Inlier. The results of this study conflict with that

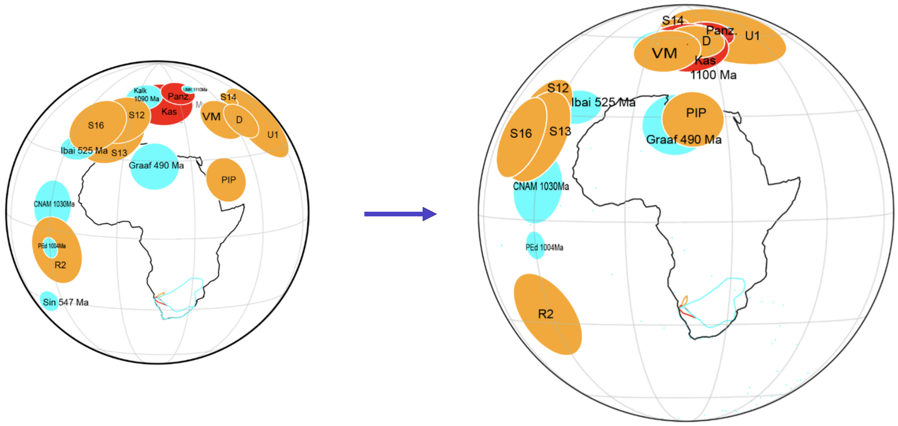

Figure 46: Proposed block rotation of Mai, 2021 and Chung-Halpern, 2021.

interpretation, and syn-folding magnetizations are not necessarily indicative of true paleomagnetic directions. Additionally, the results rely on no flattening factor f having been applied to their studies *or* the ca. 482 Graafwater Formation pole. If an f-factor is applied, as it was for the Torsvik et al., 2012 APWP, the Graafwater pole no longer overlaps with the Doornpoort post-fold pole of Piper, 1975 (Fig. 47). Therefore, the argument that the direction of the Piper, 1975 pole is due to Damaran-age magentization falls apart in the context of a large-scale block rotation. If the rotation occurred there is an overlap with this study's Leeuberg Member pole (noting that Leeuberg Member data is widely scattered and therefore not necessarily the most meaningful subset of data from this study) - but this still leaves the anomalous Piper, 1975 post-folding pole unaccounted for. Applying an f-factor to the Doornpoort syn-fold and Opdam syn-fold poles would push them closer to the equator and would require a more significant rotation to force the syn-folding poles to align with Kalahari's apparent polar wander path. If that was the case, one would expect such a significant, large-scale rotation to be somehow recorded in the geologic record.

While the author is not convinced that the paleomagnetic directions presented in this study are primary, the author tentatively suggests that it is technically possible they have not been overprinted given the conflicting lines of evidence. For the purposes of this study, two alternative conclusions are presented: a fully-folded overprint interpretation and a fully-tilt-corrected interpretation.

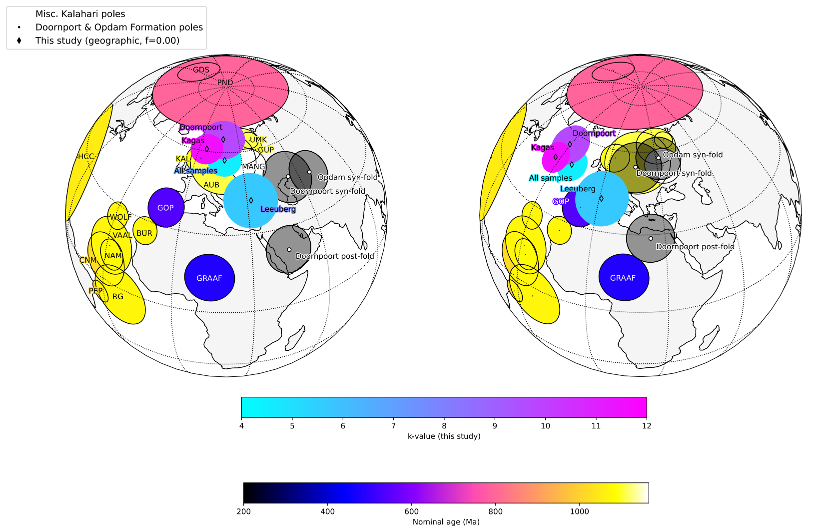

Figure 47: Model for proposed block rotation of Mai, 2021 and Chung-Halpern, 2021 in the context of this study. Non-rotated poles on left. Reference poles available in Tbl. 53.

4.1 Post-folding Magnetization Interpretation

It has not been shown in the literature whether it is appropriate to apply a flattening factor to sedimentary rocks that have been overprinted. Logically, it is not - chemical remanent magnetization (CRM) should not be subject to the same inclination shallowing as detrital remanent magnetization (DRM). A study has shown that CRM in non-overprinted rocks is not flattened and DRM is (Pierce et al., 2022). However, the author is not aware of any studies that have tested whether rocks that are fully overprinted should have a flattening factor f applied (vs. the CRM in Pierce et al., 2022 which is interpreted as having been acquired very shortly after deposition). This data set appears more Fisherian in distribution when unflattened, and the lithologies of this study have likely suffered significantly more metamorphism and/or diagenesis than the pristine lithologies of Pierce et al., 2022. For these reasons, this study presents post-folding poles that have had f applied and post-folding poles that have not had f applied. $f = 0.00$ poles from this study are shown in Fig. 48 and $f = 0.59$ poles from this study are shown in Fig. 49. In each case, three poles are presented (all of which have had their natural south-seeking polarities reversed to be north-seeking): a pole produced from all samples, a pole produced from Kagas Member samples, and a pole produced from Doornpoort Member samples. This was done due to the negative fold test results from the Doornpoort Member, indeterminate results from the Kagas Member, and combined indeterminate results from a Doornpoort and Kagas member fold test. Many of the sites within the Leeuberg Member that lies between the Doornpoort and the Kagas were widely scattered, and therefore no specific Leeuberg Member pole is presented in those figures. “All

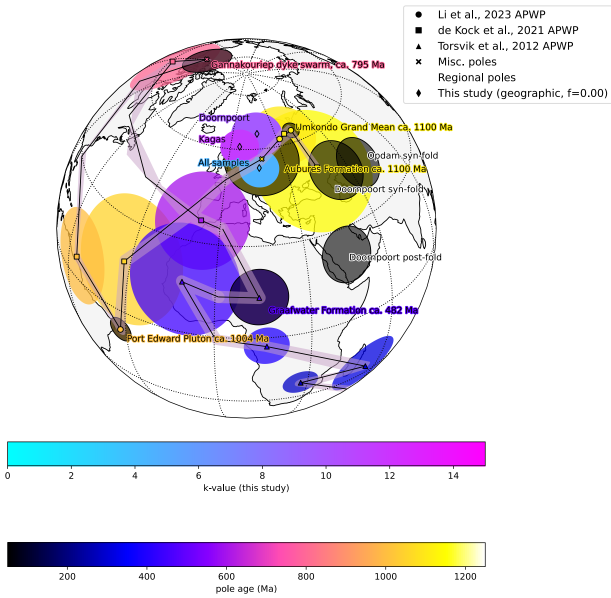

Figure 48: Post-folding interpretation. Geographic coordinates, $f = 0.00$.

samples" is defined here as any sample with MAD $\leq 15°$ that does not share a mean with the present local field (e.g., sites 23 and 25) and is not from the conglomerate test site.

All six post-folding poles overlap with the ca. 1100 Ma pole of Kasbohm et al., 2016 and trend slightly towards the low-latitude ca. 1050 Ma smoothed aggregate pole of de Kock et al., 2021. They do not overlap with the ca. 1100 Ma Umkondo LIP grand mean pole of Swanson-Hysell et al., 2015. This is interpreted as these samples having been magnetized after 1100 Ma but before 1050 Ma, if an overprint interpretation is correct.

The interpretation of this magnetization as "post-folding" is problematic in the context of the geologic record. Muscovite from the Klein Aub area (less than 50 kilometers from this study - that site and this study are approximately equidistant to the Damara front) is dated at 530 ± 10 Ma as a determination for peak-metamorphism regionally (Ahrendt et al., 1978). That date is coincident with the Damara orogeny. Maximum regional metamorphism temperature of 350° has been shown by illite crystallinity studies (Ahrendt et al., 1978). However, the directions presented in this study are in no way consistent with Damara age magnetization with (Fig. 50) or without (Fig. 48) the rotation suggested by Mai, 2021 and Chung-Halpern, 2021. In fact, no Euler pole rotation could make these poles coincide with Damara-era poles regardless of the unflattened latitude for the ca. 482 Graafwater Formation pole presented in Torsvik et al., 2012 or the flattened latitude version of the same pole presented in Mai, 2021. If some previously unidentified post-Namaqua-Natal and pre-Damara folding event occurred that magnetized these samples (while the Damara folding did *not*), the folding event would logically be expected to be strong enough to be reflected geologically

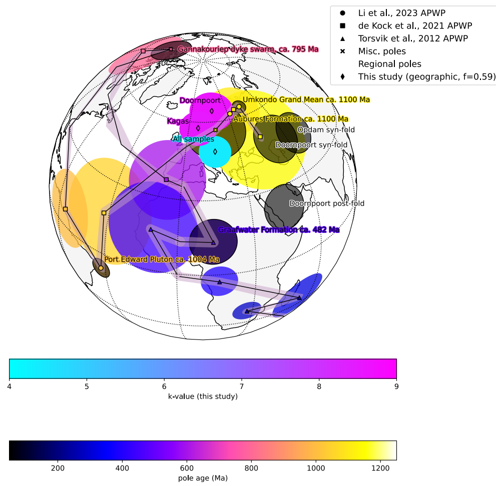

Figure 49: Post-folding interpretation. Geographic coordinates, $f = 0.59$.

(i.e., in cleavage and in the muscovite of Ahrendt et al., 1978), yet it is not. All cleavage measured for this study and shown on geologic maps is consistent with having been caused by Damara-age folding, though it is possible that pre-Damara cleavage was overprinted. That interpretation begs the question why the cleavage was overprinted during the Damara and the paleomagnetic directions were not, if these post-folding directions are indicative of some pre-Damara overprinting event. Of course, holes can also be poked in how meaningful a 1978 study is in a modern context to begin with.

If, instead, this post-folding result was related to the Namaqua-Natal folding - despite the syn-folding result of Kasbohm et al., 2016 much closer to the orogenic front (e.g., not consistent with the model of Fig. 51, Stamatakos et al., 1996) - syn-folding or pre-folding results would be expected given where these results plot on the apparent polar wander path. So, this conclusion does not simultaneously fit with both the geologic and paleomagnetic evidence, either.

Regardless, if the Damara orogen is the reason these rocks are folded (as suggested by the geologic record), failing the fold test does not make sense in the context of the VGPs developed in this study. The directions do not plot on the Phanerozoic apparent polar wander path, with or without any local Euler rotation indicative of a micro-block rotation of the Rehoboth Basement Inlier (Fig. 50, Fig. 47). Vector component mixing is certainly something to be wary of, yet many of these samples exhibit single-component behavior that is decidedly not Cambrian or present local field in direction. If rotated (Fig. 47), the post-folding poles produced from this study could lie between ca. 795 Ma poles and ca. 542 Ma poles *or* between ca. 1100 Ma and 1000 Ma poles. Neither of those are post-Damara folding, despite geologic indications

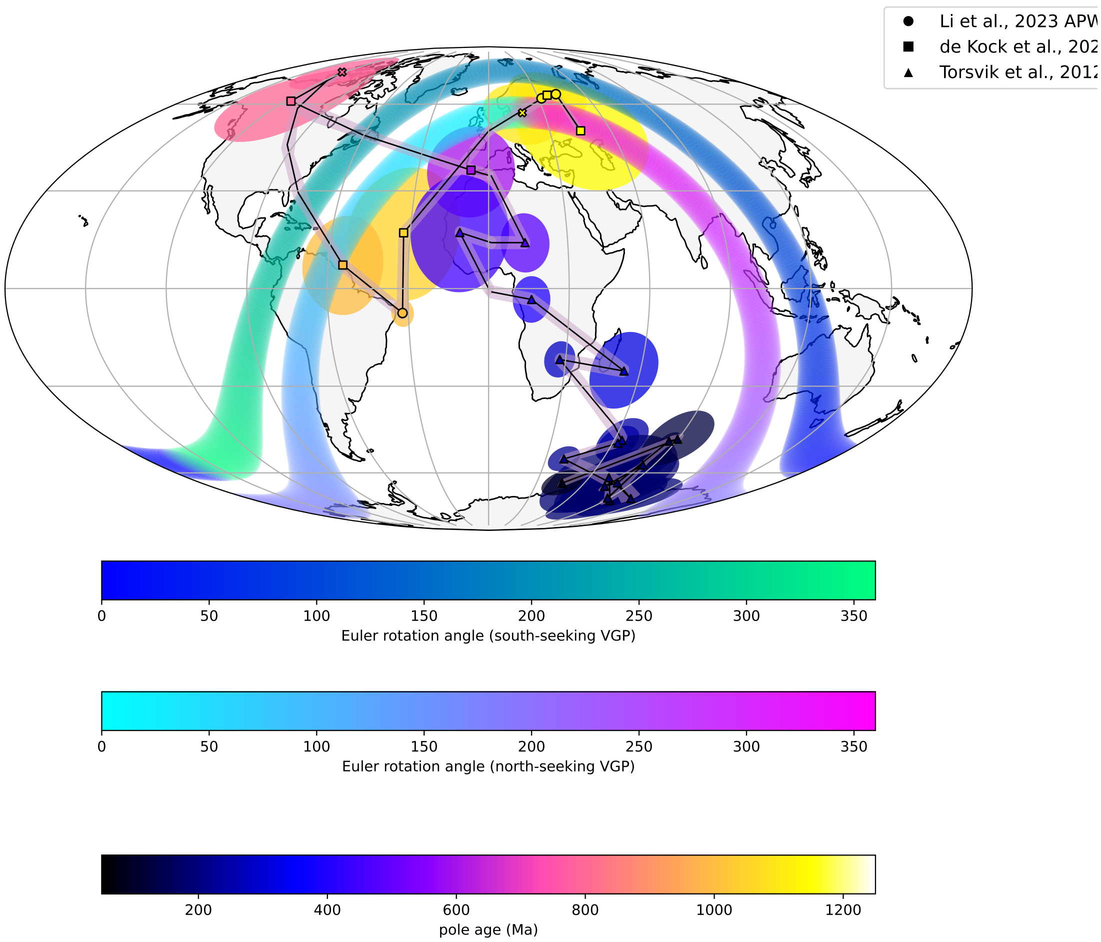

Figure 50: Post-folding interpretation. Geographic coordinates, $f = 0.00$. (24°S, 17°E, 0-360°) Euler pole rotations for study VGP as north-seeking and south-seeking showing no overlap with Damara-age Kalahari/South Africa poles.

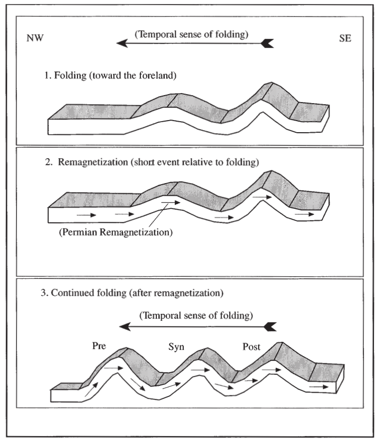

Figure 51: Cartoon model for remagnetization during Appalachian folding.

of "folding" implying Damara-era folding. When not rotated, they coincide with ca. 1100 Ma poles, but the poles of Mai, 2021 and Chung-Halpern, 2021 would now coincide with Kalahari's pre-1100 Ma APWP - which, given that the Doornpoort and Opdam formations were deposited after Umkondo-era (ca. 1100 Ma) magmatic activity had ceased, is unlikely.

So, in the case of a post-folding magnetization, this study is left to either conclude that the Damara orogen was not the predominant cause of folding in the area, which is in conflict with geologic evidence, or, the directions are meaningless altogether in the context of the age constraints and stratigraphic order of this study, Mai, 2021, and Chung-Halpern, 2021 - given that no possible model is viable when the data of this study is interpreted as overprinted (i.e., geographic coordinates and $f = 0.00$) and the data of Mai, 2021 and Chung-Halpern, 2021 is interpreted as primary. If the poles are not rotated, then the poles of Mai, 2021 and Chung-Halpern, 2021 will plot on the Kalahari APWP for units that are older than the units of Mai, 2021 and Chung-Halpern, 2021, and yet when they are rotated, the data from this study moves to a direction that is not meaningful in the context of having been overprinted. There is no way for this model to work, given the age constraints of the sampled units.

Yet there are paleomagnetic directions in the study of Chung-Halpern, 2021 from Swartkoppies dykes within the Rehoboth Basement Inlier that give *exactly* the expected Cambrian overprint direction of non-RBI-but-within-Kalahari overprinted Gannakouriep dykes when *not* rotated and give a different direction when subjected to the rotation invoked in Mai, 2021 and Chung-Halpern, 2021 (Fig. 52).

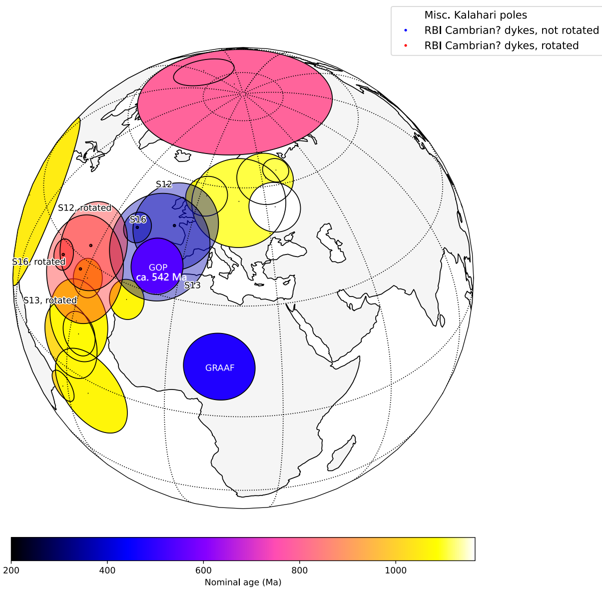

Figure 52: Paleomagnetic directions from suspected Cambrian-magnetized dykes (Chung-Halpern, 2021) not rotated (in blue) and rotated (in red). GOP = Gannakouriep dyke overprint, ca. 542 Ma.

Name	Nickname	Nordic Grade	Nominal Age	Craton	Plat	Plon	A95	Reference
Graafwater Formation	GRAAF	??	ca. 482 Ma	South Africa	13.9	13.8	9.0	Bachtadse et al, 1987
Gannakouriep overprint	GOP	C	ca. 542 Ma	Kalahari	36.7	352.0	7.0	Onstott et al, 1986
Pre-Nama dykes	PND	C	ca. 795 Ma	Kalahari	85.1	227.5	25.1	Piper, 1975
Gannakouriep dyke swarm	GDS	??	ca. 795 Ma	Kalahari	73.7	237.8	7.7	Bartholomew et al, 2008
Port Edward pluton	PEP	B	ca. 1005 Ma	Natal	-7.4	327.8	4.4	Gose et al 2004; Jacobs et al, 1997
Central Namaqua metamorphic rocks	CNM	??	ca. 1015 Ma	Kalahari	8.0	330.0	10.0	Onstott et al., 1986; Powell et al., 2001
Hlagothi Complex C	HCC	C	ca. 1050 Ma	Kalahari	20.5	281.8	22.9	Gumsley et al, 2014
Riembreek gneiss	RG	C	ca. 1070 Ma	Kalahari	-4.1	337.5	12.2	Anderson and Hattingh, 1989
Burton's Puts charnockite	BUR	C	ca. 1070 Ma	Kalahari	26.2	345.6	5.0	Anderson and Hattingh, 1989
Wolfkraal charnockite	WOLF	C	ca. 1070 Ma	Kalahari	26.3	331.0	4.9	Anderson and Hattingh, 1989
Vaalputs Formation	VAAL	C	ca. 1070 Ma	Kalahari	14.5	331.5	10.5	Anderson and Hattingh, 1989
Namaqua Belt post-tectonic mean	NAM	C	ca. 1078 Ma	Kalahari	11.6	333.1	5.7	de Kock et al., 2021; Onstott et al., 1986; Muller et al, 1978; Piper, 1975; Cornell et al., 2012
Kalkpunt Formation	KAL	C	ca. 1092 Ma	Kalahari	57.0	3.0	5.3	Briden et al., 1979; Petterson et al., 2007
Post-Guperas dykes	GUP	A	ca. 1105 Ma	Kalahari	62.3	31.9	7.1	Panzik et al., 2016
Aubures Formation	AUB	C	ca. 1108 Ma	Kalahari	56.4	18.0	11.8	Kasbohm et al., 2016
Umkondo grand mean	UMK	A	ca. 1110 Ma	Kalahari	64.0	38.8	3.3	Swanson-Hysell et al, 2015
Kalahari manganese ores	MANG	C	ca. 1165 Ma	Kalahari	54.4	33.7	6.5	Evans et al., 2001

Figure 53: List of poles as referenced in figures.

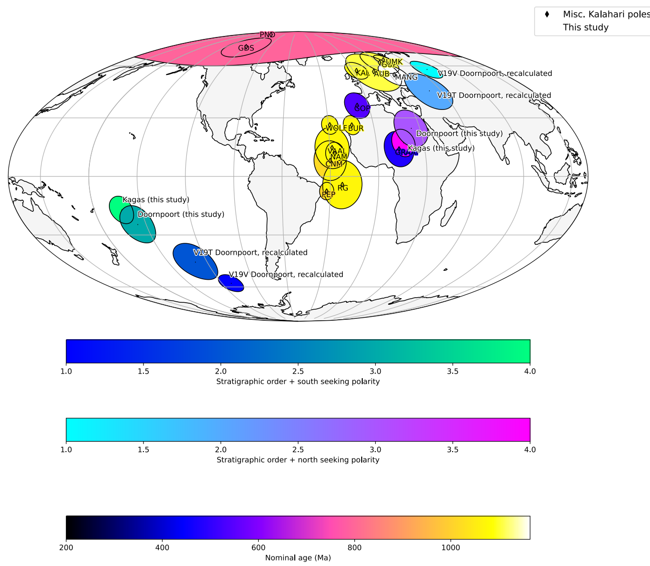

Figure 54: Paleomagnetic poles from Chung-Halpern, 2021, recalculated, and this study, tilt-corrected, $f = 0.59$. No Euler rotation applied.

4.2 Primary Magnetization Interpretation

As noted above, there are compelling reasons to believe that the most significant structural disruption in the area was due to Damara-age tectonics. Additionally, the emplacement of copper (i.e., when fluid was flowing and CRM overprint would be most likely to have happened) in the region is thought to have happened late in the region's deformation history, during basin inversion, metamorphism, and end stages of orogeny (Maiden and Borg, 2011; Sillitoe et al., 2010).

Non-rotated poles from this study and re-calculated poles (tilt-corrected and a flattening factor $f = 0.59$ applied to Doornpoort Formation sites) from Mai, 2021 yield directions that still do not fit within the context of what is currently known about Kalahari's apparent polar wander path (Fig. 54). However, they do record something meaningful by clearly maintaining stratigraphic order and "moving" in a consistent direction.

When rotated about an Euler pole, no consistent degree of rotation applied to all poles (this study and recalculated Mai, 2021 and Piper, 1975 data) is seen to "best-fit" the data (Fig. 55). So, if the negative folding test is interpreted as unconvincing and the positive Watson conglomerate test is taken at face value, a different model is required than the blanket 25-30° rotation invoked in Mai, 2021 and Chung-Halpern, 2021. Notably, the Piper, 1975 requires the same 50° rotation as the V19T sites of Mai, 2021 to be in the Cambrian overprint APWP. The V19T and Piper sites are geographically closest in comparison to any other sites included in this study. Additionally, they are likely rough stratigraphic equivalents of each other. The site furthest to the north, V19V, requires the least amount of rotation - 15° - to "best fit" the Kalahari

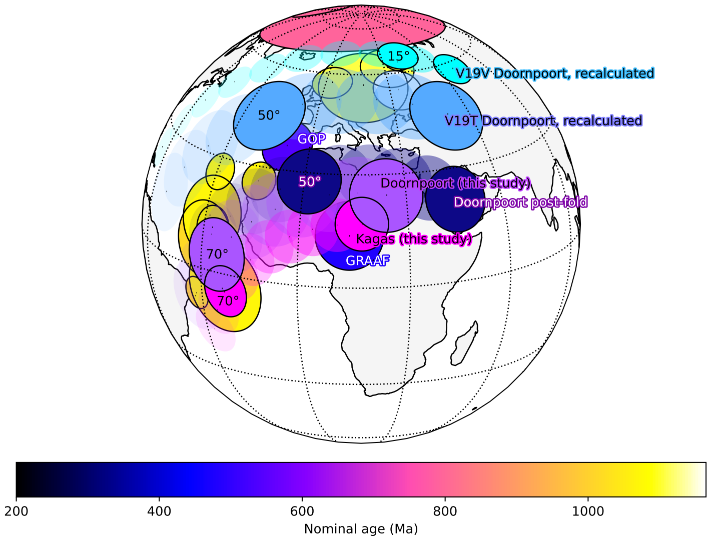

Figure 55: Paleomagnetic poles from Chung-Halpern, 2021 (recalculated). This study, tilt-corrected, $f = 0.59$. "Best fit" rotations to match with Kalahari's established APWP.

apparent polar wander path and the sites furthest to the south. The Kagas and Doornpoort of this study, require the largest rotation of 70° for "best fit" with the Kalahari apparent polar wander path. There would be a small amount of overlap at a 50° or 60° degree rotation.

This is, perhaps, the most parsimonious solution. The V19V site, as the stratigraphically lowest site, would be expected to be about ca. 1100 Ma in age given the age constraints on these formations. If rotations are *geographically* small, then the paleomagnetic poles make some sense in context with the geology, as a wrench fault system has been described in the literature (Fig. 56, note the 100m scale). Additionally, the varied degree of rotation needed for "best fit" of the poles to the established 1100 to 1000 Ma is precisely what the geology of the wrench fault system would predict. Borg et al., 1987 identified structural features in the Klein Aub area that are commonly associated with wrench faults:

1. Bedding-parallel main fault and a number of sub-parallel, minor faults.

2. En echelon folds.

3. Axial planar cleavage in some areas.

4. En echelon normal faults.

5. Extensional fractures.

6. Thrusts.

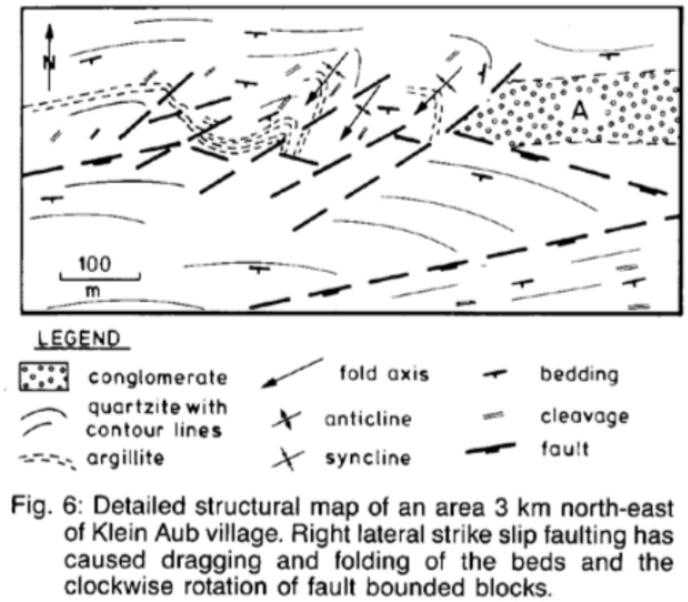

Figure 56: Structural interpretation of Borg et al., 1987. Note 100m scale.

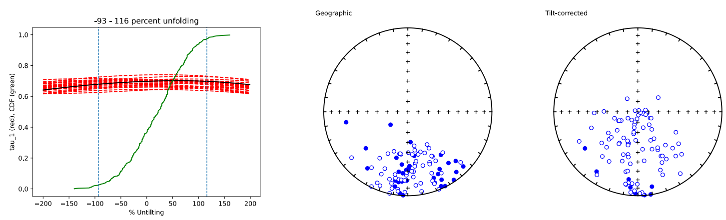

Figure 57: Indeterminate fold test, Doornpoort and Kagas only.

7. Dragging of beds at opposite ends of the fault.

Wrench faults are known for their complicated kinematics, and complex kinematics - such as rotations about multiple axes - can render fold tests meaningless (Moody and Hill, 1956). Additionally, the varied degree of rotation needed for “best fit” of the poles to the established 1100 to 1000 Ma is precisely what the geology of the wrench fault system would predict. .

5 Conclusions and Future Work

With many caveats, it is the interpretation that the results presented in this study and Mai, 2021 are primary in nature and can be interpreted meaningfully in the context of the Kalahari craton’s established apparent polar wander path. The general line of reasoning is as follows:

1. **There is no viable model in which the work of Chung-Halpern, 2021 and Mai, 2021 can**

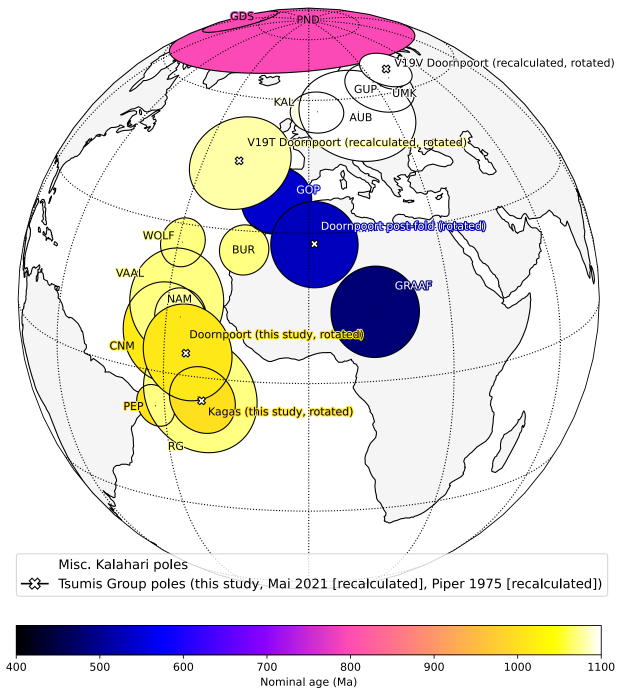

Figure 58: Recalculated paleomagnetic poles from the Tsumis Group (Mai, 2021, Piper, 1975) and this study. Tilt-corrected, $f = 0.59$. "Chi-by-eye" nominal ages assigned in the context of the Kalahari apparent polar wander path.

be interpreted as either syn-folding or primary and this study can be interpreted as overprinted. It would require the data of Chung-Halpern, 2021 and Mai, 2021 to be hundreds of millions of years older than 1100 Ma, which it is not, or the data of this study to have no overlap with the well-established Phanerozoic apparent polar wander path for Kalahari - which is unlikely given the Damara orogen having been geologically recorded as the most significant structural disruption in the area (Fig. 47).

2. The kinematically complex wrench fault system is thought to be Damara in age; thus, there is **no conflict between paleomagnetic and geologic inferences if the fold test results of this study and Mai, 2021 are interpreted as being due to structural complications** and not necessarily timing of magnetization (Fig. 56). The varied clockwise rotations in the wrench fault system is perfectly reflected in the varied counterclockwise rotations needed to correct and "best fit" the data to the 1100 to 1000 Ma Kalahari apparent polar wander path. Additionally, there are also likely more meaningful ways to perform a less-naive fold test that use more structural constraints (either already established in the literature or via a novel approach) - unfortunately, such an interpretation is not currently within the scope of this study due to the natural time constraints of a senior thesis.

Name	Plat	Plon	A95	k	Probable Age of Magnetization
Doornpoort post-fold (rotated)	27.8	1.3	8.7	58.3	530
Kagas (this study, rotated)	-4.9	338.3	7.0	11.3	1000
Doornpoort (this study, rotated)	4.6	334.9	9.7	6.6	1010
V19T Doornpoort (recalculated, rotated)	44.5	340.4	10.4	31.6	1080
V19V Doornpoort (recalculated, rotated)	66.5	41.9	5.4	24.9	1100

Figure 59: List of poles. This study, recalculated Piper, 1975, and recalculated Mai, 2021.

3. When the highly scattered, larger grain-sized Leeuberg Member data is removed, and the bootstrap fold test is re-done on only the Doornpoort Formation and Kagas Member samples, **the fold test becomes indeterminate** (Fig. 57).

4. The Shipunov conglomerate test was performed prior to the full context of the study, and may yield different results with the Leeuberg Member removed from consideration. However, **the novel approach of performing multiple conglomerate tests on the same data set, with differing angular cut-offs between samples from the same clast, could lead to be a more nuanced interpretation of conglomerate tests given a sufficient number of double-sampled clasts.** (Fig. 35; Fig. 36; Fig. 37; Fig. 38; Tbl. 3; Tbl. 2).

5. In clastic sedimentary rocks (i.e., red beds), overprinted data would be expected not to need a flattening factor f; yet this study numerically found that $f = 0.59$ was the correct approximation for this data. In fact, **this data suggests that the E/I method can be used as a meaningful field test for clastic sedimentary rocks,** particularly if rotations about multiple axes are suspected (Fig. 11). However, this idea needs to be significantly further developed and tested, though the empirical work on inclination shallowing of Pierce et al., 2022 agrees with this inference.

6. **The data does not fall on the Kalahari craton's Phanerozoic apparent polar wander path** when interpreted as post-folding (i.e., geographic coordinates and $f = 0.00$), regardless of any Rehoboth Basement Inlier rotation or smaller-scale wrench fault rotations (Fig. 50).

7. Perhaps most importantly, **the data behaves near-perfectly in context - likely recording up to 100 million years of Kalahari apparent polar wander from the bottom to the top of a 4km thick stratigraphic sequence** (Fig. 54; Fig. 55; Fig. 58).

The apparent polar wander path for Kalahari between ca. 1100 Ma and 1000 Ma has been invoked as either representing rapid true polar wander or the Kalahari craton itself rotating at low latitudes (Evans, 2003; Kaiser et al., 2016; Swanson-Hysell et al., 2015). While this study does not answer that question, nor the larger question about Kalahari's placement in Rodinia, it does suggest that with correct structural control via detailed geologic mapping, sampling further up section will yield meaningful data for the precise time period that lacks "high-quality", published paleomagnetic poles (1000 Ma to 500 Ma). However, gaining this level of structural detail will likely be difficult or impossible given the (lack of) availability of outcrop in the area.

Taking a more optimistic line of thinking, it is also possible (and suggested by satellite imagery) that the local rotation will be somewhat consistent heading further up section via the seasonal drainage sampled in this study - meaning that a 70° rotation could be applied to further data from this specific area. While the field campaign of July 2023 did not go further south due to rocks appearing reduced (i.e., green and likely of a mineralogical composition that is not suitable for paleomagnetic study), satellite imagery shows that a few kilometers further up section returns to the red color that signifies hematite-rich siliciclastics. It is therefore likely that further paleomagnetic sampling in this region, combined with as rigorous an approach to geologic mapping as is possible, could answer the long-debated "Kalahari-in-Rodinia" question.

References

Ahrendt, H., Hunziker, J. C., & Weber, K. (1978). Age and degree of metamorphism and time of nappe emplacement along the southern margin of the Damara Orogen/Namibia (SW-Africa). *Geologische Rundschau*, *67*(2), 719–742. https://doi.org/10.1007/BF01802814

Asefaw, H., Tauxe, L., Koppers, A. a. P., & Staudigel, H. (2021). Four-Dimensional Paleomagnetic Dataset: Plio-Pleistocene Paleodirection and Paleointensity Results From the Erebus Volcanic Province, Antarctica. *Journal of Geophysical Research: Solid Earth*, *126*(2), e2020JB020834. https://doi.org/10.1029/2020JB020834

Bartholomew, L. T. (2008). *Paleomagnetism of Neoproterozoic intraplate igneous rocks in the southwest Kalahari Craton, Namibia and South Africa* [Master's thesis, Texas Christian University].

Becker, T., Garoeb, H., Ledru, P., & Milesi, J.-P. (2005). The Mesoproterozoic event within the Rehoboth Basement Inlier of Namibia: Review and new aspects of stratigraphy, geochemistry, structure and plate tectonic setting. *South African Journal of Geology*, *108*(4), 465–492. https://doi.org/10.2113/108.4.465

Becker, T., & Schalk, K. (2008). Sinclair Supergroup and associated intrusive rocks. *Miller, R. McG.(Ed.), The Geology of Namibia: Archaean to Mesoproterozoic*, *1*, 8–68.

Biggin, A. J., van Hinsbergen, D. J., Langereis, C. G., Straathof, G. B., & Deenen, M. H. (2008). Geomagnetic secular variation in the Cretaceous Normal Superchron and in the Jurassic. *Physics of the Earth and Planetary Interiors*, *169*(1-4), 3–19.

Borg, B. (1986). Stratabound copper-silver-gold mineralization of late proterozoic age along the margin of the Kalahari Craton in Southwest Africa/Namibia and Botswana. *Canadian Mineralogist*, *24*, 178.

Borg, G., Graf, N., & Maiden, K. J. (1987). The Klein Aub Fault Zone - A Wrench Fault System in Middle Proterozoic Metasediments in Central SWA/Namibia.

Borg, G. (1987). Controls on Stratabound Copper Mineralization at Klein Aub Mine and Similar Deposits within the Kalahari Copperbelt of South West Mrica/Namibia and Botswana.

Borg, G., & Maiden, K. (1989). The Middle Proterozoic Kalahari copperbelt of Namibia and Botswana. *Geological Association of Canada Special Paper*, *36*, 525–540.

Burger, A., & Coertze, F. (1975). Age determinations-April 1972 to March 1974. *Annals of the Geological Survey of South Africa*, *10*, 135–141.

Butler, R. F. (2004). *Magnetic Domains to Geologic Terranes.*

Cairanne, G., Aubourg, C., & Pozzi, J.-P. (2002). Syn-folding remagnetization and the significance of the small circle test: Examples from the Vocontian trough (SE France). *Physics and Chemistry of the Earth, Parts A/B/C*, *27*(25-31), 1151–1159.

Cawood, P. A., & Pisarevsky, S. A. (2017). Laurentia-Baltica-Amazonia relations during Rodinia assembly. *Precambrian Research*, *292*, 386–397. https://doi.org/10.1016/j.precamres.2017.01.031

Cawood, P. A., Strachan, R. A., Pisarevsky, S. A., Gladkochub, D. P., & Murphy, J. B. (2016). Linking collisional and accretionary orogens during Rodinia assembly and breakup: Implications for models of supercontinent cycles. *Earth and Planetary Science Letters*, *449*, 118–126. https://doi.org/10.1016/j.epsl.2016.05.049

Chung-Halpern, C. (2021). *Reconnaissance Paleomagnetism of the Northern Rehoboth Basement Inlier, Namibia* [undergrad].

Corner, B., & Durrheim, R. J. (2018). An Integrated Geophysical and Geological Interpretation of the Southern African Lithosphere. In S. Siegesmund, M. A. S. Basei, P. Oyhantçabal, & S. Oriolo (Eds.), *Geology of Southwest Gondwana* (pp. 19–61). Springer International Publishing. https://doi.org/10.1007/978-3-319-68920-3_2

Cox, G. M., Halverson, G. P., Stevenson, R. K., Vokaty, M., Poirier, A., Kunzmann, M., Li, Z.-X., Denyszyn, S. W., Strauss, J. V., & Macdonald, F. A. (2016). Continental flood basalt weathering as a trigger for Neoproterozoic Snowball Earth. *Earth and Planetary Science Letters*, *446*, 89–99. https://doi.org/10.1016/j.epsl.2016.04.016

Dalziel, I. W. (1997). Overview: Neoproterozoic-Paleozoic geography and tectonics: Review, hypothesis, environmental speculation. *Geological Society of America Bulletin*, *109*(1), 16–42.

de Kock, M. O., Evans, D. A. D., & Beukes, N. J. (2009). Validating the existence of Vaalbara in the Neoarchean. *Precambrian Research*, *174*(1), 145–154. https://doi.org/10.1016/j.precamres.2009.07.002

de Kock, M. O., Luskin, C. R., Djeutchou, C., & Wabo, H. (2021, January). Chapter 12 - The Precambrian drift history and paleogeography of the Kalahari Craton. In L. J. Pesonen, J. Salminen, S.-Å. Elming, D. A. D. Evans, & T. Veikkolainen (Eds.), *Ancient Supercontinents and the Paleogeography of Earth* (pp. 377–422). Elsevier. https://doi.org/10.1016/B978-0-12-818533-9.00019-9

Delaunay, S., Smith, B., & Aubourg, C. (2002). Asymmetrical fold test in the case of overfolding: Two examples from the Makran accretionary prism (Southern Iran). *Physics and Chemistry of the Earth, Parts A/B/C*, *27*(25-31), 1195–1203.

Ding, J., Zhang, S., Evans, D. A., Yang, T., Li, H., Wu, H., & Chen, J. (2021). North China craton: The conjugate margin for northwestern Laurentia in Rodinia. *Geology*, *49*(7), 773–778. https://doi.org/10.1130/G48483.1

Donnadieu, Y., Goddéris, Y., Ramstein, G., Nédélec, A., & Meert, J. (2004). A 'snowball Earth' climate triggered by continental break-up through changes in runoff. *Nature*, *428*(6980), 303–306. https://doi.org/10.1038/nature02408

Dufour, F., Davies, J. H., Greenman, J. W., Skulski, T., Halverson, G. P., & Stevenson, R. (2023). New U-Pb CA-ID TIMS zircon ages implicate the Franklin LIP as the proximal trigger for the Sturtian Snowball Earth event. *Earth and Planetary Science Letters*, *618*, 118259. https://doi.org/10.1016/j.epsl.2023.118259

Dunlop, D. J., & Özdemir, Ö. (1997). *Rock magnetism: Fundamentals and frontiers*. Cambridge university press.

Ernst, R., Gladkochub, D., Söderlund, U., Donskaya, T., Pisarevsky, S., Mazukabzov, A., & El Bilali, H. (2023). Identification of the ca. 720 Ma Irkutsk LIP and its plume centre in southern Siberia: The initiation of Laurentia-Siberia separation. *Precambrian Research*, *394*, 107111.

Evans, D. A. D. (2003). True polar wander and supercontinents. *Tectonophysics*, *362*(1), 303–320. https://doi.org/10.1016/S0040-1951(02)000642-X

Evans, D. A. D. (2021, January). Chapter 17 - Meso-Neoproterozoic Rodinia supercycle. In L. J. Pesonen, J. Salminen, S.-Å. Elming, D. A. D. Evans, & T. Veikkolainen (Eds.), *Ancient Supercontinents and the Paleogeography of Earth* (pp. 549–576). Elsevier. https://doi.org/10.1016/B978-0-12-818533-9.00006-0

Evans, D. A. D., Veselovsky, R. V., Petrov, P. Y., Shatsillo, A. V., & Pavlov, V. E. (2016). Paleomagnetism of Mesoproterozoic margins of the Anabar Shield: A hypothesized billion-year partnership of Siberia and northern Laurentia. *Precambrian Research*, *281*, 639–655. https://doi.org/10.1016/j.precamres.2016.06.017

Evans, D. A. (2000). Stratigraphic, geochronological, and paleomagnetic constraints upon the Neoproterozoic climatic paradox. *American Journal of Science*, *300*(5), 347–433.

Eyster, A., Fu, R. R., Strauss, J. V., Weiss, B. P., Roots, C. F., Halverson, G. P., Evans, D. A., & Macdonald, F. A. (2017). Paleomagnetic evidence for a large rotation of the Yukon block relative to Laurentia: Implications for a low-latitude Sturtian glaciation and the breakup of Rodinia. *GSA Bulletin*, *129*(1-2), 38–58. https://doi.org/10.1130/B31425.1

Eyster, A., Weiss, B. P., Karlstrom, K., & Macdonald, F. A. (2020). Paleomagnetism of the Chuar Group and evaluation of the late Tonian Laurentian apparent polar wander path with implications for the makeup and breakup of Rodinia. *GSA Bulletin*, *132*(3-4), 710–738. https://doi.org/10.1130/B32012.1

Fisher, N., Lewis, T., & Embleton, B. J. J. (1993, August). *Statistical Analysis of Spherical Data*. Cambridge University Press.

Fisher, R. A. (1953). Dispersion on a sphere. *Proceedings of the Royal Society of London. Series A. Mathematical and Physical Sciences*, *217*(1130), 295–305. https://doi.org/10.1098/rspa.1953.0064

Gerritsen, D., Vaes, B., & van Hinsbergen, D. J. J. (2022). Influence of Data Filters on the Position and Precision of Paleomagnetic Poles: What Is the Optimal Sampling Strategy? *Geochemistry, Geophysics, Geosystems*, *23*(4), e2021GC010269. https://doi.org/10.1029/2021GC010269

Gerya, T. (2014). Precambrian geodynamics: Concepts and models. *Gondwana Research*, *25*(2), 442–463. https://doi.org/10.1016/j.gr.2012.11.008

Goddéris, Y., Donnadieu, Y., Nédélec, A., Dupré, B., Dessert, C., Grard, A., Ramstein, G., & François, L. M. (2003). The Sturtian 'snowball' glaciation: Fire and ice. *Earth and Planetary Science Letters*, *211*(1), 1–12. https://doi.org/10.1016/S0012-821X(03)00197-3

Graham, J. W. (1949). The stability and significance of magnetism in sedimentary rocks. *Journal of Geophysical Research (1896-1977)*, *54*(2), 131–167. https://doi.org/10.1029/JZ054i002p00131

Gumsley, A. P., de Kock, M., Ernst, R., Gumsley, A., Hanson, R., Kamo, S., Knoper, M., Lewandowski, M., Luks, B., Mamuse, A., & Söderlund, U. (2023). The Mutare-Fingeren Dyke Swarm: The enigma of the Kalahari Craton's exit from supercontinent Rodinia. *eological Society, London, Special Publications*, *537*(1).

Hanson, R. E., Harmer, R. E., Blenkinsop, T. G., Bullen, D. S., Dalziel, I. W. D., Gose, W. A., Hall, R. P., Kampunzu, A. B., Key, R. M., Mukwakwami, J., Munyanyiwa, H., Pancake, J. A., Seidel, E. K., & Ward, S. E. (2006). Mesoproterozoic intraplate magmatism in the Kalahari Craton: A review. *Journal of African Earth Sciences*, *46*(1), 141–167. https://doi.org/10.1016/j.jafrearsci.2006.01.016

Hanson, R. E., Crowley, J. L., Bowring, S. A., Ramezani, J., Gose, W. A., Dalziel, I. W. D., Pancake, J. A., Seidel, E. K., Blenkinsop, T. G., & Mukwakwami, J. (2004). Coeval Large-Scale Magmatism in the Kalahari and Laurentian Cratons During Rodinia Assembly. *Science*, *304*(5674), 1126–1129. https://doi.org/10.1126/science.1096329

Heslop, D., & Roberts, A. P. (2018). A Bayesian Approach to the Paleomagnetic Conglomerate Test. *Journal of Geophysical Research: Solid Earth*, *123*(2), 1132–1142. https://doi.org/10.1002/2017JB014526

Hoffman, P. F. (1991). Did the Breakout of Laurentia Turn Gondwanaland Inside-Out? *Science*, *252*(5011), 1409–1412. https://doi.org/10.1126/science.252.5011.1409

Hoffman, P. F. (1999). The break-up of Rodinia, birth of Gondwana, true polar wander and the snowball Earth. *Journal of African Earth Sciences*, *28*(1), 17–33. https://doi.org/10.1016/S0899-5362(99)00018-4

Hoffman, P. F. (2021). On the kinematics and timing of Rodinia breakup: A possible rift–transform junction of Cryogenian age at the southwest cape of Congo Craton (northwest Namibia). *South African Journal of Geology*, *124*(2), 401–420. https://doi.org/10.25131/sajg.124.0038

Hoffman, P. F., Abbot, D. S., Ashkenazy, Y., Benn, D. I., Brocks, J. J., Cohen, P. A., Cox, G. M., Creveling, J. R., Donnadieu, Y., Erwin, D. H., Fairchild, I. J., Ferreira, D., Goodman, J. C., Halverson, G. P., Jansen, M. F., Le Hir, G., Love, G. D., Macdonald, F. A., Maloof, A. C., … Warren, S. G. (2017). Snowball Earth climate dynamics and Cryogenian geology-geobiology. *Science Advances*, *3*(11), e1600983. https://doi.org/10.1126/sciadv.1600983

Hoffman, P. F., Kaufman, A. J., Halverson, G. P., & Schrag, D. P. (1998). A Neoproterozoic Snowball Earth. *Science*, *281*(5381), 1342–1346. https://doi.org/10.1126/science.281.5381.1342

Hoffmann, K. (1989). New aspects of lithostratigraphic subdivision and correlation of late Profiter-ozoic to early Cambrian rocks of the southern Damara Belt and their corre-lation with the central and northern Damara Belt and the Gariep Belt. *Commun. Geol. Surv. Namibia*, *5*, 61–70.

Jacobs, J., Pisarevsky, S., Thomas, R. J., & Becker, T. (2008). The Kalahari Craton during the assembly and dispersal of Rodinia. *Precambrian Research*, *160*(1), 142–158. https://doi.org/10.1016/j.precamres.2007.04.022

Jagoutz, O., Macdonald, F. A., & Royden, L. (2016). Low-latitude arc–continent collision as a driver for global cooling. *Proceedings of the National Academy of Sciences*, *113*(18), 4935–4940. https://doi.org/10.1073/pnas.1523667113

Jing, X., Evans, D. A., Yang, Z., Tong, Y., Xu, Y., & Wang, H. (2020). Inverted South China: A novel configuration for Rodinia and its breakup. *Geology*, *49*(4), 463–467. https://doi.org/10.1130/G47807.1

Jing, X., Evans, D. A., Yang, Z., Tong, Y., Xu, Y., & Wang, H. (2021). Inverted South China: A novel configuration for Rodinia and its breakup. *Geology*, *49*(4), 463–467. https://doi.org/10.1130/G47807.1

Johnson, C. L., Constable, C. G., Tauxe, L., Barendregt, R., Brown, L. L., Coe, R. S., Layer, P., Mejia, V., Opdyke, N. D., Singer, B. S., Staudigel, H., & Stone, D. B. (2008). Recent investigations of the 0–5 Ma geomagnetic field recorded by lava flows. *Geochemistry, Geophysics, Geosystems*, *9*(4). https://doi.org/10.1029/2007GC001696

Kaiser, S. I., Aretz, M., & Becker, R. T. (2016). The global Hangenberg Crisis (Devonian–Carboniferous transition): Review of a first-order mass extinction. *Geological Society, London, Special Publications*, *423*(1), 387–437. https://doi.org/10.1144/SP423.9

Kasbohm, J., Evans, D. A. D., Panzik, J. E., Hofmann, M., & Linnemann, U. (2016). Palaeomagnetic and geochronological data from Late Mesoproterozoic redbed sedimentary rocks on the western margin of Kalahari craton. *Geological Society, London, Special Publications*, *424*(1), 145–165. https://doi.org/10.1144/SP424.4

Kent, D. V. (1985). Thermoviscous remagnetization in some Appalachian limestones. *Geophysical Research Letters*, *12*(12), 805–808. https://doi.org/10.1029/GL012i012p00805

Kent, D. V., & Miller, J. D. (1987). Redbeds and thermoviscous magnetization theory. *Geophysical Research Letters*, *14*(4), 327–330. https://doi.org/10.1029/GL014i004p00327

Kirschvink, J. L. (1980). The least-squares line and plane and the analysis of palaeomagnetic data. *Geophysical Journal International*, *62*(3), 699–718. https://doi.org/10.1111/j.1365-246X.1980.tb02601.x

Kirschvink, J. L. (1992). Late Proterozoic low-latitude global glaciation : The Snowball Earth. *The Proterozoic Biosphere*.

Lee, C.-T. A., Thurner, S., Paterson, S., & Cao, W. (2015). The rise and fall of continental arcs: Interplays between magmatism, uplift, weathering, and climate. *Earth and Planetary Science Letters*, *425*, 105–119. https://doi.org/10.1016/j.epsl.2015.05.045

Lehmann, J., Master, S., Rankin, W., Milani, L., Kinnaird, J. A., Naydenov, K. V., Saalmann, K., & Kumar, M. (2015). Regional aeromagnetic and stratigraphic correlations of the Kalahari Copperbelt in Namibia and Botswana. *Ore Geology Reviews*, *71*, 169–190. https://doi.org/10.1016/j.oregeorev.2015.05.009

Li, Z. X., Mitchell, R. N., Spencer, C. J., Ernst, R., Pisarevsky, S., Kirscher, U., & Murphy, J. B. (2019). Decoding Earth's rhythms: Modulation of supercontinent cycles by longer superocean episodes. *Precambrian Research*, *323*, 1–5. https://doi.org/10.1016/j.precamres.2019.01.009

Li, Z.-X., Bogdanova, S. V., Collins, A. S., Davidson, A., De Waele, B., Ernst, R. E., Fitzsimons, I. C. W., Fuck, R. A., Gladkochub, D. P., Jacobs, J., Karlstrom, K. E., Lu, S., Natapov, L. M., Pease, V., Pisarevsky, S. A., Thrane, K., & Vernikovsky, V. (2008). Assembly, configuration, and break-up history of Rodinia: A synthesis. *Precambrian Research*, *160*(1), 179–210. https://doi.org/10.1016/j.precamres.2007.04.021

Li, Z.-X., Evans, D. A. D., & Halverson, G. P. (2013). Neoproterozoic glaciations in a revised global palaeogeography from the breakup of Rodinia to the assembly of Gondwanaland. *Sedimentary Geology*, *294*, 219–232. https://doi.org/10.1016/j.sedgeo.2013.05.016

Li, Z., Liu, Y., & Ernst, R. (2023). A dynamic 2000—540Ma Earth history: From cratonic amalgamation to the age of supercontinent cycle. *Earth-Science Reviews*, *238*, 104336. https://doi.org/10.1016/j.earscirev.2023.104336

Lippert, P. C., van Hinsbergen, D. J., & Dupont-Nivet, G. (2014). Early Cretaceous to present latitude of the central proto-Tibetan Plateau: A paleomagnetic synthesis with implications for Cenozoic tectonics, paleogeography, and climate of Asia. *Geological Society of America Special Papers*, *507*, 1–21.

Macdonald, F. A., Schmitz, M. D., Crowley, J. L., Roots, C. F., Jones, D. S., Maloof, A. C., Strauss, J. V., Cohen, P. A., Johnston, D. T., & Schrag, D. P. (2010). Calibrating the Cryogenian. *Science*, *327*(5970), 1241–1243. https://doi.org/10.1126/science.1183325

Macdonald, F. A., & Swanson-Hysell, N. L. (2023). The Franklin Large Igneous Province and Snowball Earth Initiation.

Macdonald, F. A., Swanson-Hysell, N. L., Park, Y., Lisiecki, L., & Jagoutz, O. (2019). Arc-continent collisions in the tropics set Earth's climate state. *Science*, *364*(6436), 181–184. https://doi.org/10.1126/science.aav5300

Mai, V. V. (2021). *Paleomagnetic regional survey of late magmatic & sedimentary of the Southern Rehoboth Basement Inlier* [undergrad].

Maiden, K. J., & Borg, G. (2011). The Kalahari Copperbelt in Central Namibia: Controls on copper mineralization. *SEG Newsletter*, (87), 1–19.

Mardia, K. V. (1975). Statistics of directional data. *Journal of the Royal Statistical Society Series B: Statistical Methodology*, *37*(3), 349–371.

Master, S., Kasirye, S., & Master, R. (2014). Microbially-induced sand cracks (polygonal petee ridges) in an early Neoproterozoic siliciclastic foreshore setting, Doornpoort Formation, Sinclair Supergroup (Rehoboth, Namibia).

McCabe, C., & Elmore, R. D. (1989). The occurrence and origin of Late Paleozoic remagnetization in the sedimentary rocks of North America. *Reviews of Geophysics*, *27*(4), 471–494. https://doi.org/10.1029/RG027i004p00471

McElhinny, M. W., & Merrill, R. T. (1975). Geomagnetic secular variation over the past 5 m.y. *Reviews of Geophysics*, *13*(5), 687–708. https://doi.org/10.1029/RG013i005p00687

McElhinny, M. W., & McFadden, P. L. (1999). *Paleomagnetism: Continents and oceans*. Elsevier.

Meert, J. G. (2012). The (Paleo) geography of evolution: Making sense of changing biology and changing continents. *Evolution: Education and Outreach*, *5*, 547–554.

Meert, J. G., Pivarunas, A. F., Evans, D. A. D., Pisarevsky, S. A., Pesonen, L. J., Li, Z.-X., Elming, S.-Å., Miller, S. R., Zhang, S., & Salminen, J. M. (2020). The magnificent seven: A proposal for modest revision of the Van der Voo (1990) quality index. *Tectonophysics*, *790*, 228549. https://doi.org/10.1016/j.tecto.2020.228549

Meert, J. G., & Torsvik, T. H. (2003). The making and unmaking of a supercontinent: Rodinia revisited. *Tectonophysics*, *375*(1), 261–288. https://doi.org/10.1016/S0040-1951(03)00342-1

Merdith, A. S., Collins, A. S., Williams, S. E., Pisarevsky, S., Foden, J. D., Archibald, D. B., Blades, M. L., Alessio, B. L., Armistead, S., Plavsa, D., Clark, C., & Müller, R. D. (2017). A full-plate global reconstruction of the Neoproterozoic. *Gondwana Research*, *50*, 84–134. https://doi.org/10.1016/j.gr.2017.04.001

Merdith, A. S., Williams, S. E., Müller, R. D., & Collins, A. S. (2017). Kinematic constraints on the Rodinia to Gondwana transition. *Precambrian Research*, *299*, 132–150.

Miller, R. M. (2012). REVIEW OF MESOPROTEROZOIC MAGMATISM, SEDIMENTATION AND TERRANE AMALGAMATION IN SOUTHWESTERN AFRICA. *South African Journal of Geology*, *115*(4), 417–448. https://doi.org/10.2113/gssajg.115.4.417

Miller, R. M., & Becker, T. (2008). *The Geology of Namibia: Archaean to mesoproterozoic*. Ministry of Mines; Energy, Geological Survey.

Mitchell, R. N., Zhang, N., Salminen, J., Liu, Y., Spencer, C. J., Steinberger, B., Murphy, J. B., & Li, Z.-X. (2021). The supercontinent cycle. *Nature Reviews Earth & Environment*, *2*(5), 358–374. https://doi.org/10.1038/s43017-021-00160-0

Moody, J., & Hill, M. (1956). WRENCH-FAULT TECTONICS. *GSA Bulletin*, *67*(9), 1207–1246. https://doi.org/10.1130/0016-7606(1956)67[1207:WT]2.0.CO;2

Oliver, J. (1986). Fluids expelled tectonically from orogenic belts: Their role in hydrocarbon migration and other geologic phenomena. *Geology*, *14*(2), 99. https://doi.org/10.1130/0091-7613(1986)14⟨99:FETFOB⟩2.0.CO;2

Opdyke, M. D., & Channell, J. E. T. (1996, November). *Magnetic Stratigraphy*. Academic Press.

Pfurr, N., Ahrendt, H., Hansen, B. T., & Weber, K. (1991). U-Pb and Rb-Sr isotopic study of granitic gneisses and associated metavol- canic rocks from the Rostock massifs, southern margin of the Damara Orogen: Implications for lithostratigraphy of this crustal segment.

Pierce, J., Zhang, Y., Hodgin, E., & Swanson-Hysell, N. (2022). Quantifying Inclination Shallowing and Representing Flattening Uncertainty in Sedimentary Paleomagnetic Poles. *Geochemistry, Geophysics, Geosystems*, *23*. https://doi.org/10.1029/2022GC010682

Piper, J. D. A. (1975). The Palaeomagnetism of Precambrian Igneous and Sedimentary Rocks of the Orange River Belt in South Africa and South West Africa. *Geophysical Journal International*, *40*(3), 313–344. https://doi.org/10.1111/j.1365-246X.1975.tb04135.x

Pisarevsky, S. A., Wingate, M. T. D., Powell, C. M., Johnson, S., & Evans, D. A. D. (2003). Models of Rodinia assembly and fragmentation. *Geological Society, London, Special Publications*, *206*(1), 35–55. https://doi.org/10.1144/GSL.SP.2003.206.01.04

Pu, J. P., Macdonald, F. A., Schmitz, M. D., Rainbird, R. H., Bleeker, W., Peak, B. A., Flowers, R. M., Hoffman, P. F., Rioux, M., & Hamilton, M. A. (2022). Emplacement of the Franklin large igneous province and initiation of the Sturtian Snowball Earth. *Science Advances*, *8*(47), eadc9430. https://doi.org/10.1126/sciadv.adc9430

Pu, J. P., Macdonald, F. A., Smith, E. F., Ramezani, J., & Swanson-Hysell, N. (2023). Tonian basins record rifting of Kalahari from Rodinia and no evidence of a pre-Sturtian Kaigas glaciation. *Earth and Planetary Science Letters*, *624*, 118472. https://doi.org/10.1016/j.epsl.2023.118472

Reid, D. L., Malling, S., & Alisopp, H. L. (1988). Rb-Sr AGES OF GRANITOIDS IN THE REHOBOTH-NAUCHAS AREA, SOUTH WEST AFRICA/NAMIBIA.

Rose, I., & Buffett, B. (2017). Scaling rates of true polar wander in convecting planets and moons. *Physics of the Earth and Planetary Interiors*, *273*, 1–10. https://doi.org/10.1016/j.pepi.2017.10.003

Ruxton, P. (1986). *Sedimentology, isotopic signature and ore genesis of the Klein Aub Copper Mine, South West Africa/Namibia*. Geological Society of South Africa.

Ruxton, P. A. (1981). *The sedimentology and diagenesis of copper-bearing rocks of the southern margin of the Damaran Orogenic Belt, Namibia and Botswana* [phd]. University of Leeds.

Schneider, T., Becker, T., Borg, G., Hilken, U., Hansen, B. T., & Weber, K. (2004). New U-Pb zircon ages of the Nückopf Formation and their significance.

Seifert, N. (1986). Geochronologische Untersuchungen an Basement-Gesteinen am Südrand des Damara-Orogens (Namibia). *Geochronologische Untersuchungen an Basement-Gesteinen am Südrand des Damara-Orogens (Namibia)*, *66*(3), 483–484.

Shipunov, S. V., Muraviev, A. A., & Bazhenov, M. L. (1998). A new conglomerate test in palaeomagnetism. *Geophysical Journal International*, *133*(3), 721–725. https://doi.org/10.1046/j.1365-246X.1998.00516.x

Sillitoe, R. H., Perelló, J., & García, A. (2010). Sulfide-Bearing Veinlets Throughout the Stratiform Mineralization of the Central African Copperbelt: Temporal and Genetic Implications. *Economic Geology*, *105*(8), 1361–1368. https://doi.org/10.2113/econgeo.105.8.1361

Stamatakos, J., Hirt, A. M., & Lowrie, W. (1996). The age and timing of folding in the central Appalachians from paleomagnetic results. *Geological Society of America Bulletin*, *108*(7), 815–829. https://doi.org/10.1130/0016-7606(1996)108⟨0815:TAATOF⟩2.3.CO;2

Starkey, J., & Palmer, H. C. (1971). The Sensitivity of the Conglomerate Test in Palaeomagnetism. *Geophysical Journal of the Royal Astronomical Society*, *22*(3), 235–240. https://doi.org/10.1111/j.1365-246X.1971.tb03596.x

Stoessel, G. F. U., & Ziegler, U. R. F. (1989). Report: Geochemical, Rb-Sr and V-Pb isotope studies of some acid volcanics from the Rehoboth Basement Inlier, Namibia.

Suppe, J. (1983). Geometry and kinematics of fault-bend folding. *American Journal of science*, *283*(7), 684–721.

Swanson-Hysell, N. L. (2021, January). Chapter 4 - The Precambrian paleogeography of Laurentia. In L. J. Pesonen, J. Salminen, S.-Å. Elming, D. A. D. Evans, & T. Veikkolainen (Eds.), *Ancient Supercontinents and the Paleogeography of Earth* (pp. 109–153). Elsevier. https://doi.org/10.1016/B978-0-12-818533-9.00009-6

Swanson-Hysell, N., Kilian, T., & Hanson, R. (2015). A new grand mean palaeomagnetic pole for the 1.11 Ga Umkondo large igneous province with implications for palaeogeography and the geomagnetic field. *Geophysical Journal International*, *203*(3), 2237–2247. https://doi.org/10.1093/gji/ggv402

Tauxe, L., Shaar, R., Jonestrask, L., Swanson-Hysell, N. L., Minnett, R., Koppers, A. a. P., Constable, C. G., Jarboe, N., Gaastra, K., & Fairchild, L. (2016). PmagPy: Software package for paleomagnetic data analysis and a bridge to the Magnetics Information Consortium (MagIC) Database. *Geochemistry, Geophysics, Geosystems*, *17*(6), 2450–2463. https://doi.org/10.1002/2016GC006307

Tauxe, L., & Watson, G. S. (1994). The fold test: An eigen analysis approach. *Earth and Planetary Science Letters*, *122*(3), 331–341. https://doi.org/10.1016/0012-821X(94)90006-X

Tauxe, L. (2005). Inclination flattening and the geocentric axial dipole hypothesis. *Earth and Planetary Science Letters*, *233*(3-4), 247–261.

Tauxe, L. (2010). *Essentials of Paleomagnetism*. University of California Press.

Tauxe, L., & Kent, D. V. (1984). Properties of a detrital remanence carried by haematite from study of modern river deposits and laboratory redeposition experiments. *Geophysical Journal International*, *76*(3), 543–561. https://doi.org/10.1111/j.1365-246X.1984.tb01909.x

Tauxe, L., Kylstra, N., & Constable, C. (1991). Bootstrap statistics for paleomagnetic data. *Journal of Geophysical Research: Solid Earth*, *96*(B7), 11723–11740. https://doi.org/10.1029/91JB00572

Torsvik, T. H., Van der Voo, R., Preeden, U., Mac Niocaill, C., Steinberger, B., Doubrovine, P. V., van Hinsbergen, D. J. J., Domeier, M., Gaina, C., Tohver, E., Meert, J. G., McCausland, P. J. A., & Cocks, L. R. M. (2012). Phanerozoic polar wander, palaeogeography and dynamics. *Earth-Science Reviews*, *114*(3), 325–368. https://doi.org/10.1016/j.earscirev.2012.06.007

Vaes, B., Li, S., Langereis, C. G., & van Hinsbergen, D. J. J. (2021). Reliability of palaeomagnetic poles from sedimentary rocks. *Geophysical Journal International*, *225*(2), 1281–1303. https://doi.org/10.1093/gji/ggab016

Vandamme, D. (1994). A new method to determine paleosecular variation. *Physics of the Earth and Planetary Interiors*, *85*(1), 131–142. https://doi.org/10.1016/0031-9201(94)90012-4

Villalaín, J., Fernández-González, G., Casas, A., & Gil-Imaz, A. (2003). Evidence of a Cretaceous remagnetization in the Cameros Basin (North Spain): Implications for basin geometry. *Tectonophysics*, *377*(1-2), 101–117.

Watkins, N. (1973). Brunhes epoch geomagnetic secular variation on Reunion Island. *Journal of Geophysical Research*, *78*(32), 7763–7768.

Watson, G. S. (1956). A Test for Randomness of Directions. *Geophysical Supplements to the Monthly Notices of the Royal Astronomical Society*, *7*(4), 160–161. https://doi.org/10.1111/j.1365-246X.1956.tb05561.x

Wilson, R., Dagley, P., & McCormack, A. (1972). Palaeomagnetic evidence about the source of the geomagnetic field. *Geophysical Journal International*, *28*(2), 213–224.

Yu, Y., & Tauxe, L. (2006). Acquisition of viscous remanent magnetization. *Physics of the Earth and Planetary Interiors*, *159*(1), 32–42. https://doi.org/10.1016/j.pepi.2006.05.002

Zahirovic, S., Müller, R. D., Seton, M., & Flament, N. (2015). Tectonic speed limits from plate kinematic reconstructions. *Earth and Planetary Science Letters*, *418*, 40–52. https://doi.org/10.1016/j.epsl.2015.02.037

Zhao, G., Wang, Y., Huang, B., Dong, Y., Li, S., Zhang, G., & Yu, S. (2018). Geological reconstructions of the East Asian blocks: From the breakup of Rodinia to the assembly of Pangea. *Earth-Science Reviews*, *186*, 262–286.

Ziegler, U. R. F., & Stoessel, G. F. U. (1993). *Age Determinations in the Rehoboth Basement Inlier, Namibia.* Geological Survey of Namibia, Ministry of Mines; Energy.